



**HAL**  
open science

# Effect of Welding Microstructure on Stress Relaxation Cracking Studied by Controlled Residual Stress Generation in a 316L(N) Austenitic Stainless Steel

Baptiste Py-Renaudie, Diogo Goncalves, Serge Pascal, Mohamed Sennour, Vladimir A. Esin, Thilo F. Morgeneyer

► **To cite this version:**

Baptiste Py-Renaudie, Diogo Goncalves, Serge Pascal, Mohamed Sennour, Vladimir A. Esin, et al.. Effect of Welding Microstructure on Stress Relaxation Cracking Studied by Controlled Residual Stress Generation in a 316L(N) Austenitic Stainless Steel. Metallurgical and Materials Transactions A, 2023, 10.1007/s11661-023-07182-x . hal-04236188

**HAL Id: hal-04236188**

**<https://hal.science/hal-04236188>**

Submitted on 10 Oct 2023

**HAL** is a multi-disciplinary open access archive for the deposit and dissemination of scientific research documents, whether they are published or not. The documents may come from teaching and research institutions in France or abroad, or from public or private research centers.

L'archive ouverte pluridisciplinaire **HAL**, est destinée au dépôt et à la diffusion de documents scientifiques de niveau recherche, publiés ou non, émanant des établissements d'enseignement et de recherche français ou étrangers, des laboratoires publics ou privés.

Effect of welding microstructure on stress relaxation cracking by controlled residual stress generation in a 316L(N) austenitic stainless steel

16/09/2022

Baptiste PY-RENAUDIE <sup>1,2,\*</sup>, Diogo GONCALVES <sup>1</sup>, Serge Pascal <sup>1</sup>, Mohamed SENNOUR <sup>2</sup>, Vladimir A. ESIN <sup>2</sup>, Thilo F. MORGENEYER <sup>2</sup>

<sup>1</sup> Service d'Études Mécaniques et Thermiques (SEMT), CEA, Université Paris-Saclay, F-91191 Gif-Sur-Yvette, France

<sup>2</sup> Mines Paris, PSL University, Centre for material sciences (MAT), UMR7633 CNRS, F-91003 Evry Cedex, France

\*Corresponding author: Service d'Études Mécaniques et Thermiques (SEMT), CEA, Université Paris-Saclay, Gif-Sur-Yvette, France.

E-mail adress : baptiste.py-renaudie@cea.fr

## Abstract

The influence of heterogeneous welding microstructure on the stress relaxation cracking (SRC) in the SRC-resistant 316L(N) steel was investigated. To trigger SRC, pre-straining by compression was applied after the welding and before subsequent stress relaxation by heat treatment. To this end, compact tension (CT) type specimens were extracted from thick plates welded on both sides. The notch was aligned with the welding centreline and notch root across the thickness, thereby crossing the heterogeneous microstructure. Residual stresses and strain fields induced by welding and pre-compression were estimated by 3D finite element simulations and values of the same order of magnitude were obtained for all regions of the weld. After thermal heat treatment at 575 °C for 580 and 1470 h of the welded and further pre-strained CT samples, intergranular cavities and cracks similar to those found after the creep were observed. Cavities appeared exclusively on intergranular carbides and associated intermetallic precipitates. In the fusion zone (FZ), cavities preferentially nucleated on phases issued from the decomposition of the vermicular ferrite formed during welding. The highest number of cracks was systematically found in the coarse grain heat affected zone (CGHAZ) of the weld. An increase in both pre-compression load and relaxation time led to an increase in damage after the heat treatment.

Keywords: 316L(N) stainless steels; welding; stress relaxation cracking; reheat cracking; stress relief cracking; residual stress; heat-affected zone, finite element simulations; creep cavity nucleation.

## 1) Introduction

The 4th generation nuclear reactors, namely Sodium-cooled Fast Reactors (SFR), are intended to be continuously exposed to temperatures of the order of 550 °C during the service lifetime [1]. Such conditions are favorable to stress relaxation cracking (SRC) issues observed in welded components made from austenitic stainless steels. SRC in austenitic stainless steels and nickel-base alloys, also referred as “stress relief cracking”, “stress induced cracking”, “reheat cracking” and “strain age cracking” has been extensively studied since the 1950s. High carbon steels, as the 304, 304H, 316, 316H, 800, 800H, 800HT alloys [2-9], and stabilized austenitic stainless steels, such as the 347 and 321 grades [10-12], appeared to be particularly sensitive to SRC indicating an important carbon effect, i.e. that of carbides. However, no industrial case of SRC was reported for low carbon steels such as the 316L(N) steel. Recent studies confirmed its low sensitivity to SRC [13]. Such a SRC resistance together with good mechanical properties make the 316L(N) steel an optimal material for primary and secondary circuits components of the nuclear reactors of new generation. Nevertheless, failure induced by SRC during long term service of 316L(N) might be expected and should be thus correctly predicted.

According to the literature, SRC of welded components during service is initiated by three main factors:

(i) work hardening before service, which induces a reduction in ductility but also increases precipitation kinetics of carbides and intermetallics [14-17]. The work hardening of welded components is primary due to the heat cycles induced by the welding, but may also be induced by cold working applied to the material prior to service;

(ii) precipitation of secondary phases both in the bulk and at grain boundaries (GBs) due to high temperature exposure during service. Precipitation in the bulk, mainly observed in high carbon steels, induces the hardening of the grain volume, leading to the localization of plastic strain at GBs [18-21]. GB precipitation further restricts the ability of grain boundaries to accommodate strain [22]. Additionally, grain boundary precipitates act as nucleation sites for creep-like GB cavities because of strain incompatibility with the matrix and dislocation pile-up, resulting in stress concentration [20].

(iii) relaxation of residual stresses found in the zones affected by welding, emerging during the cooling after welding [13, 16, 17, 22, 23]. In some cases, the material cannot withstand inelastic strain imposed by stress relaxation in the heat-affected regions during service at high temperature, leading to cracking [9, 17, 20, 22, 24-28].

Other factors were identified as increasing the susceptibility to failure during stress relaxation: the geometry and thickness of the components [2, 5, 7, 9, 19, 22, 24, 27, 29, 30], the steel composition, with the particularly harmful effect of molybdenum, vanadium, carbon and boron known to facilitate carbide precipitation [22, 24], niobium [16] and nitrogen [13] which also slows down the stress relaxation kinetics [13, 17, 20]. Coarse grains are also often reported to be detrimental for the resistance to SRC [7, 19, 22, 31-34]. Generally, it is admitted that steels with grain size larger than 130  $\mu\text{m}$  present a higher risk of SRC, although SRC was reported as well in steels with grain size as small as 65  $\mu\text{m}$  [7, 35].

Generally, factors such as work hardening, residual stresses and grain size of affected zones can be largely influenced by the weld design, technique and procedure. Besides, secondary phase precipitation may also occur during the welding process, particularly in high-carbon and stabilized steels.

The cracks formed during the relaxation of the welded parts were predominantly observed just below the fusion zone (FZ), in the coarse grain heat-affected zone (CGHAZ), and generally initiated at the toe of the weld bead of failed joints [2, 3, 20, 22, 25-27, 30, 36-39]. Crack propagation was mostly reported to be parallel to the FZ/CGHAZ interface, along the grain boundaries (GB) [22, 24, 25, 38], even though Lancaster *et al.* [2] also reported the cases of cracks penetrating the HAZ and then propagating into the base metal (BM). In some rare cases, SRC was observed to develop in the FZ as well [2, 9, 37]. Observations of damaged materials revealed the presence of GB cavities, similar to those forming during creep, near the crack tip and located close to GB precipitates, mostly carbides [5, 7, 27, 28, 30, 34, 36, 40-42].

Despite numerous studies, the complexity of the SRC phenomenon and the test duration to trigger damage generally required simplifying the testing conditions and the initial state of the studied material. Therefore, to date, various approaches have been considered:

- using fully welded specimens which are representative of industrial cases, since the entire microstructure, stress and strain fields induced by welding are preserved. However, this method presents many drawbacks: bad reproducibility, difficulty of residual stress measurement and monitoring, large volume to be analyzed and impossibility to control SRC factors;

- reproducing the microstructure and properties of heat affected zones by appropriate heat treatment and/or work hardening [3, 13, 16, 17, 43]. This method is a simplification of industrial welds,

but allows an easier study because of the homogeneous microstructure. Residual stresses can be introduced applying mechanical preloads by compression of CT-like specimens or 3 point bending tests.

- using CT-like specimens in order to introduce the residual stresses present in the HAZs [23]. This approach, combined with the reproduction of a HAZ microstructure, ensures good control of the applied conditions and excellent reproducibility. The main drawback is that it does not account for the effect of a heterogeneous microstructure.

- using welded CT-like specimens [44]. This allows studying real weld microstructure under controlled applied mechanical conditions. However, the authors who adopted this approach only characterized damage in the FZ and therefore did not investigate the effect of structural heterogeneity on the SRC.

In most of these studies accounting for SRC on austenitic steels, GB cavities were not considered to quantify the damage, even though cavity nucleation is known to be at the origin of cracks by stress relaxation [5, 13, 26, 28, 40, 41]. Nevertheless, Bouchard *et al.* quantified the damage accounting for the number of cavities and characterized their distribution, allowing a finer understanding of damage initiation and development [21, 45-49].

Therefore, the present work proposes to study the effect of welding on SRC in a 316L(N) stainless steel paying special attention to GB cavities and related microstructure in order to better understand the physical mechanism governing SRC within this material. This new approach considers damage after both cavity nucleation and cracking in pre-compressed and thermally aged CT specimens accounting for heterogeneous microstructure of a welded 316L(N) stainless steel, but also by controlling the main SRC factors, as residual stress, strain and relaxation time.

To achieve that, a 316L(N) steel plate was subjected to a single-pass welding without filler metal. Then, CT-like specimens were machined from the welded plate and further compressed to introduce controlled levels of residual stresses and strain. These were estimated by finite element method simulations, accounting for the heterogeneous microstructure. Numerical simulations showed residual stresses induced by welding were erased by plastic straining during the pre-compression and could be thus neglected. Specimens were then heat treated at 575 °C to relax residual stresses, and damage was characterized through microscopy and image analysis. The influence of welding microstructure, relaxation time and pre-compression on SRC was investigated.

## 2) Material and methods

### a) Material in as-received state

The studied 316L(N) steel (Table 1) was received as plates with dimensions of 450×90×30 mm<sup>3</sup>, after austenitizing at 1100 °C for 35 min followed by water quenching. Plates were further reduced to half thickness by EDM (Electrical Discharge Machining). The details of methods used for microstructure characterization are detailed later in Section 2) d) **Microstructure and damage analyses**.

Optical and Scanning Electron Microscopy (SEM) analyses revealed the presence of residual ferrite, elongated in the rolling direction. The absence of ferrite diffraction peak suggests very low ferrite fraction, less than the XRD detection limit, i.e. less than 1% wt. Typical annealed microstructure is observed with equiaxed and no textured grains. The average grain size was estimated to be of the order of 90 µm by the average grain intercept method [REF-E112]. Neither SEM nor TEM (Transmission Electron microscopy) analyses revealed bulk or GB precipitates in as-received state.

Table 1: Chemical composition of the 316L(N) stainless steel [%wt].

| Fe | C | Cr | Ni | Mn | Mo | N | Si | P | Co | Cu | Al | Si |
|----|---|----|----|----|----|---|----|---|----|----|----|----|
|----|---|----|----|----|----|---|----|---|----|----|----|----|

|      |      |      |      |      |      |      |      |      |      |      |      |      |
|------|------|------|------|------|------|------|------|------|------|------|------|------|
| Bal. | 0.02 | 16.9 | 11.9 | 1.74 | 2.42 | 0.07 | 0.19 | 0.03 | 0.04 | 0.15 | 0.01 | 0.19 |
|------|------|------|------|------|------|------|------|------|------|------|------|------|

### b) Welding without filler metal

Before welding, the 316L(N) plate was clamped, in order to prevent any distortion during the welding and further cooling to room temperature. Then, GTAW (Gas Tungsten Arc Welding), without the deposition of filler metal, was applied along the X direction on both sides of the (XY) surface planes of the plate (Figure 1). Such process induced welding heat cycles comparable to those in industrial welds, while avoiding the influence of the filler metal on the mechanical behavior and thus sensitivity to SRC. The surface temperature between two welding passes (one for each side of the plate) was systematically lower than 100 °C, avoiding the overlapping of heat gradients. Welding was carried out with the parameters similar to industrial processes, using argon as shielding gas, voltage of 12 V, current of 300 A and an automated torch displacement rate of 60 mm/min. During the displacement, the welding torch allowed partial melting of the near-surface metal (the fusion zone) and formation of heat affected zones as in industrial welding process (Figure 1).

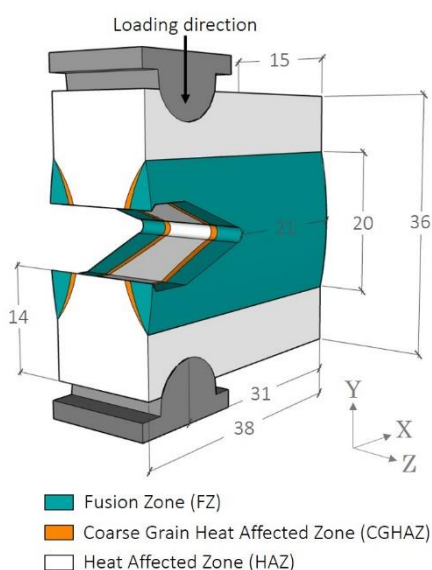


Figure 1: Scheme of welding of 316L(N) plate without filler metal by GTAW (Gas Tungsten Arc Welding) for further CT (Compact Tension) specimens machining and mechanical straining with the geometry of CT sample with compression setup loading direction (Y). Dimensions are given in mm.

### c) Controlled generation of pre-strain and residual stresses by compression

For 316L(N) steels, the residual stresses due to welding hardly exceed 500 MPa [50-52], and are supposed to be not sufficient to induce SRC in this material. Indeed, Pommier suggested an SRC threshold of 740 +/- 40 MPa for a 316L(N) steel of similar composition [13]. In order to introduce residual stresses of such magnitude and plastic strain to ensure triggering SRC, four CT specimens were machined from the as-welded plate by EDM (Figure 1). These specimens were further compressed, resulting in residual tensile stress near the notch after unloading, as shown by Turski *et al.* [23].

To carry out the pre-compression, CT-like specimens were mounted on an MTS hydraulic machine with a 250 kN load capacity and maintained between two metallic pieces presenting a round edge with the radius of the CT top and bottom cylindrical seats (Figure 1). In addition, to measure

applied force and displacement, an MTS clip extensometer was placed into the crack mouth opening of the CT samples allowing measuring the crack mouth opening displacement (CMOD). Compressions were performed at room temperature with a loading in the Y direction and displacement rate of 0.005 mm s<sup>-1</sup> until maximum imposed value of CMOD was reached. Finally, the CT samples were completely unloaded within 5 s.

After compression, both as-welded (without pre-compression, for comparison) and welded CT samples were heat treated at 575 °C for 580 and 1470 h in ambient air to allow the relaxation of residual stresses. This temperature was chosen based on the results of Pommier *et al.* [13], who found more stress relaxation damage in pre-strained 316L(N) further aged at 575 °C than those aged at 550 or 600 °C. Pommier suggested this was due to the SRC mechanism being dependent on stress relaxation behavior and GB degradation, directly linked to the composition of the tested steel (particularly, C and N content) and the temperature. At 575 °C, the time for the GB strength to be overcome by the residual stress would be lower than that at 550 and 600 °C. During the relaxation heat treatment at 575 °C, no external mechanical load was applied. Table 2 summarizes the experimental conditions applied to each specimen.

Table 2: SRC testing conditions. CMOD stands for Crack Mouth Opening Displacement.

| Specimen     | Final CMOD [mm] | Ageing temperature [°C] | Ageing time [h] |
|--------------|-----------------|-------------------------|-----------------|
| As-welded    | 0               | 575                     | 580             |
|              |                 |                         | 1470            |
| As-welded CT | 1.39            |                         | 1470            |
|              | 1.73            |                         | 1470            |
|              | 6.09            |                         | 580             |
|              | 6.41            |                         | 1470            |

#### d) Estimation of residual stresses induced by compression

The welding resulted in heterogeneous microstructure and consequently heterogeneous mechanical properties. To determine the mechanical properties of different zones of as-welded sample, 1 mm thick tensile specimens were machined from (XY) planes, in both parallel (X axis) and transverse (Y axis) directions to the welding bead. Tensile tests were carried out at room temperature using an Instron 5966 machine with a 10 kN capacity and a 0.017 mm s<sup>-1</sup> displacement rate. The results were further used to adjust the parameters of the mechanical model used for numerical simulations.

Numerical simulations using finite element modelling (FEM) were performed to predict the residual stresses generated in the notch root of the CT-like specimens after compression loading and ensure sufficient stress was present prior to relaxation to trigger SRC. These simulations were carried out under continuum mechanics hypotheses, and thus did not take into account local heterogeneities due to the microstructure (namely, grain orientation and morphology, secondary phase precipitates). The mechanical behavior of the 316L(N) steel at room temperature was modeled by the elastoplastic model proposed by Chaboche [53], accounting for both isotropic and kinematic hardening. The plasticity criterion follows the equation (1). The equation (2) describes the evolution of the cumulated plastic strain. Equations (3) and (4) describe isotropic and kinematic stresses, respectively.  $J_2$  denotes for the second principal invariant of the stress deviatoric tensor,  $\sigma$  the stress tensor,  $\mathbf{X}$  the kinematic stress tensor,  $\boldsymbol{\varepsilon}^P$  the plastic strain tensor and  $p$  the cumulated plastic strain.  $A_1$ ,  $C_2$ ,  $A_2$ ,  $C_2$ ,  $\psi$ ,  $\Omega$ ,  $b$ ,  $R_M$  and  $R_0$  are material-dependent adjustable parameters.

$$J_2(\boldsymbol{\sigma} - \mathbf{X}) = R(p) \quad (1)$$

$$\dot{p} = \sqrt{\frac{2}{3} \dot{\epsilon}^p : \dot{\epsilon}^p} \quad (2)$$

$$\dot{R} = b(R_M - R)\dot{p}, \text{ with } R(0) = R_0 \quad (3)$$

$$\mathbf{X} = \sum_i \mathbf{X}_i \quad (4)$$

$$\dot{\mathbf{X}}_i = \frac{2}{3} A_i \cdot C_i \cdot \phi(p) \cdot \dot{\epsilon}^p - C_i \cdot \mathbf{X}_i \cdot \dot{p}, \text{ with } \phi(p) = 1 + (\psi - 1)e^{-\Omega \cdot p}$$

Kinematic hardening parameters were fitted from tension-compression experimental tests data for a 316L(N) of very similar composition to the one studied, from results of Pommier [13]. The other model parameters were adjusted to fit the experimental tensile curves of each region of the welded plate. Table 3 details the adjusted parameters values, and the Young's Modulus, E, and Poisson's ratio,  $\nu$ , for each weld zone. Parameters used for the HAZ were the same as those for the as-received state. However, the work hardening of the HAZ induced by welding heat was simulated by imposing an initial cumulated plastic strain of 4%.

Table 3: Chaboche model parameters used in this work to simulate the compression tests for the as-received and welded 316L(N) steel.

| Parameter            | As-received         | Fusion Zone         |
|----------------------|---------------------|---------------------|
| E [MPa]              | 200.10 <sup>3</sup> | 200.10 <sup>3</sup> |
| $\nu$ [-]            | 0.296               | 0.296               |
| A <sub>1</sub> [MPa] | 70                  | 70                  |
| C <sub>1</sub> [-]   | 100                 | 200                 |
| A <sub>2</sub> [MPa] | 200                 | 200                 |
| C <sub>2</sub> [-]   | 2                   | 2                   |
| $\psi$ [-]           | 1.25                | 1.25                |
| $\Omega$ [-]         | 2                   | 2                   |
| R <sub>0</sub> [MPa] | 230                 | 200                 |
| R <sub>M</sub> [MPa] | 830                 | 850                 |
| b [-]                | 3                   | 2.05                |

The FEM computations were performed with the Cast3M software [54]. A 3D FEM mesh of a quarter of the CT specimen was made, composed of cubic elements with the largest elements situated in expected low strain areas of a size of 1.00 mm and the smallest elements at the notch set to a size of 0.01 mm. Numerical convergence was verified performing simulations with element sizes 10 times smaller at the notch, leading to 0.1% of difference with the coarser meshing. The FZ shape and dimensions were determined from experimental macroscopic images of sections of the welded plate. CGHAZ was not considered in the simulations due to its small thickness (less than 1.00 mm), as compared to the other two zones and to the size of the mesh.

### e) Microstructure and damage analyses

After compression and subsequent heat treatment, the CT specimens were cut by EDM at mid-thickness for analyses of the HAZ in the (XY) plane (Figure 2-1). The other halves of the specimens were further cut in the (YZ) plane 1 mm before the notch root (Figure 2-2) for analyses over the whole microstructure with the FZ, CGHAZ and HAZ. These were then mechanically ground in the (YZ) plane using SiC abrasive paper to reach the plane of notch root (Figure 2-3). Samples were further polished with diamond paste of abrasive size of 6, 3, 1  $\mu\text{m}$  and finally with a solution of colloidal silica for SEM

and EBSD analyses. In average, the final (YZ) plane of observation was located at 40  $\mu\text{m}$  distance from the notch root after polishing. This allowed investigating the damage over the heterogeneous microstructure in the plane containing highest levels of residual stress and plastic strain near the notch according to the numerical simulations (see below), thus highest probability of stress relaxation damage.

Cavities and cracks induced by stress relaxation were observed with a Zeiss Gemini Sigma 500 Scanning Electron Microscope (SEM) operating at accelerating voltage of 20 kV and using both Secondary Electrons (SE) and Backscattered Electrons (BSE) detectors. In (YZ) plane of observation, SEM images were taken along the Z-axis from the sample surface to the half thickness over a width of about 700  $\mu\text{m}$  in the Y-axis (Figure 2) to detect damage. Obtained SEM micrographs were then binarized to reveal cavities and cracks. Other defects were manually removed from the images ensuring a quantification of damage only. A black pixel count algorithm was used to determine the position of cavities/cracks and estimate their number (Figure 2). Electron Back Scatter Diffraction (EBSD) analyses were carried out using Bruker e-Flash camera and acquisition steps varying from 550 nm to 3  $\mu\text{m}$ . EBSD allowed accessing the grain structure, evaluating the strain state of different areas of welded microstructure and nature of precipitates observed after heat treatments. The strain was estimated using both Grain Orientation Spread (GOS) and Kernel Average Misorientation (KAM) methods. The GOS gives the average difference between the orientation of each pixel of a given grain and the average orientation of the same grain [55]. This method is relevant to compare strain state of different grains, zones and samples. However, it is not suitable for local strain analyses and KAM criterion should be used instead. KAM calculates the misorientation between a point and its neighbors in the kernel of the chosen size (1<sup>st</sup> neighbors were considered in this work). Analyses with a high resolution Tecnai F 20 ST Transmission Electron Microscope (TEM) were also conducted to identify the nature of secondary phase precipitates in samples extracted from the damaged specimen near the notch root. Hardening of different welded areas was estimated with Vickers hardness measurement across the cross-section of the welded plate with a 1.0 kgf using a Struers Duramin-A300 tester.

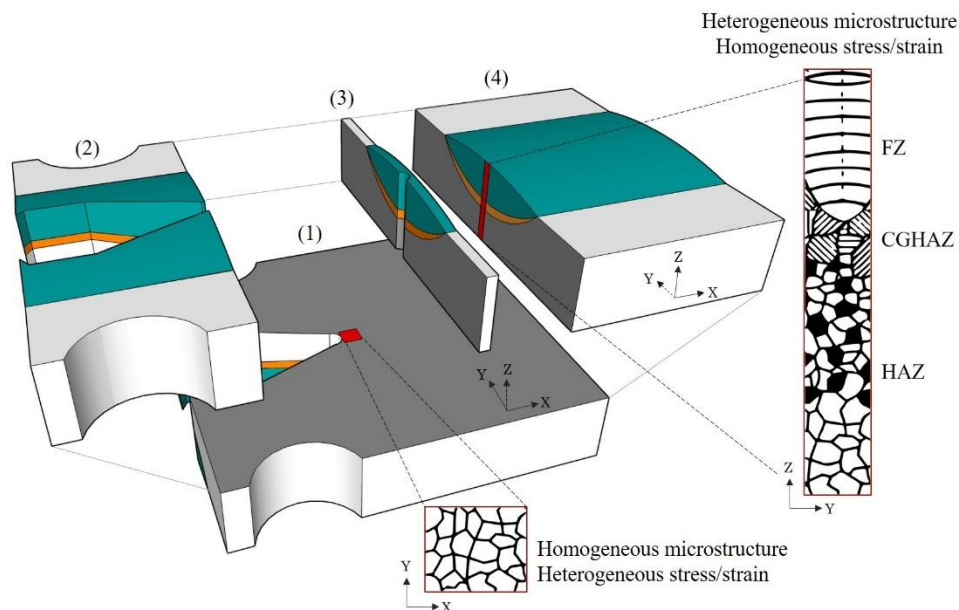


Figure 2: Damage analysis after compression and stress relaxation of CT (Compact Tension) specimens. Preparation of specimens was achieved by: (1) cutting in mid-thickness in the (XY) plane, (2) cutting near the notch in the (YZ) plane and (3) polishing to the notch. Red regions represent the regions of interest for damage analyses. FZ stands for Fusion Zone, CGHAZ for Coarse Grain Heat affected Zone, and HAZ for Heat affected Zone.

### 3) Results and discussion

#### 1) Microstructure after welding

EBSD analyses carried out in the cross-section of the welded plate (Figure 3) allowed characterizing the microstructure and estimating the strain state after the welding. According to the IPF map after single pass of welding (Figure 3 (b)), three distinct zones can be distinguished using the grain shape and size:

(i) The fusion zone (FZ), where temperatures during welding were higher than the steel melting temperature ( $T > 1400\text{ }^{\circ}\text{C}$ ). In this region, the austenitic grain morphology varied from columnar at the bottom of the FZ to mostly equiaxed near the surface. The grain size was larger (up to  $1000\text{ }\mu\text{m}$ ) than that in the as-received state. The high temperatures also allowed the formation of vermicular ferrite at the austenite grain boundaries and within the grains during the cooling. Such structures of ferrite cells are commonly observed in weld microstructure of austenitic stainless steel [56]. The hardness in this zone was found to be 137 and 163 HV1 (Figure 3 (a)), which is comparable to the 155 HV1 hardness measured for the as-received state. In this zone no significant strain can be stated, as suggested by the GOS map shown in Figure 3 (c).

(ii) The Coarse Grain Heat Affected Zone (CGHAZ) was observed just below the FZ, forming a circular band along the bottom of the FZ, being 1 mm thick at maximum at the welding centerline. In this zone, temperatures during welding were high enough to induce austenite grain growth without melting, between  $1000$  and  $1400\text{ }^{\circ}\text{C}$  [57]. Austenite grains in this region measured up to  $500\text{ }\mu\text{m}$ , with a few intergranular vermicular ferrite cells observed near the FZ/CGHAZ boundary. Residual ferrite islands in this region were mostly decomposed into several secondary phases rich in Cr and Mo. In this zone, GOS map showed very similar values to those obtained for the as-received state and the fusion zone, suggesting little to no strain. This is also consistent with low hardness, which was the lowest (close to 140 HV1) in the CGHAZ. The decrease of apparent hardness in the CGHAZ, as compared with the as-received initial state (155 HV1), might be induced by coarser grains. However, larger grain size in the FZ but higher average hardness suggests the grain size is not the only parameter that should be considered here. Decrease of hardness could also be due to the presence of tensile residual stress, as it was suggested by Pommier [13]. Typically, decrease of hardness in the CGHAZ was also observed by Jiang *et al.* [58].

(iii) Finally, Heat Affected Zone (HAZ) was observed below the CGHAZ. This HAZ was exposed to lower temperatures than the CGHAZ during welding, between  $600$  and  $1100\text{ }^{\circ}\text{C}$ , which does not lead to grain growth for the short process durations (less than a minute). Therefore, the microstructure in HAZ was very similar to that observed for the as-received state, with no phase transformation or precipitation apart from formation of small Mo-rich precipitates at some of the residual ferrite/austenite interfaces. By comparison with the as-received state, GOS map suggests an increase in strain in the HAZ, as compared to other regions, especially towards the plate mid-thickness (Figure 3 (c)). This is consistent with the hardness increase in the cross-section of the welded plate, with the highest value close to 180 HV1 found at mid-thickness at 4 to 5 mm from the FZs (Figure 3 (a)). Such a result is in agreement with the data reported by Auzoux *et al.* [17], who observed hardening due to welding in regions 15 mm far from the FZ, with highest values at 4 mm from the FZ. Observed asymmetry of the hardness profile is believed to be due to the second pass (on the second side of the plate) of welding torch taking place after the first pass (on the first side) which could affect the strain state. From these observations, it was concluded that the specimens further used for SRC tests did not contain any regions with the steel in as-received state.

Additional observations carried out using SEM did not reveal any austenite GB precipitates in the CGHAZ nor in the HAZ which is consistent with common observations for low carbons steels [59] and particularly with results found by Weiss *et al.* [14] for a 316L(N) steel with a similar chemical composition. According to them, for a similar steel the quickest precipitation of  $M_{23}C_6$  requires at least 1 h of treatment at 775 °C.

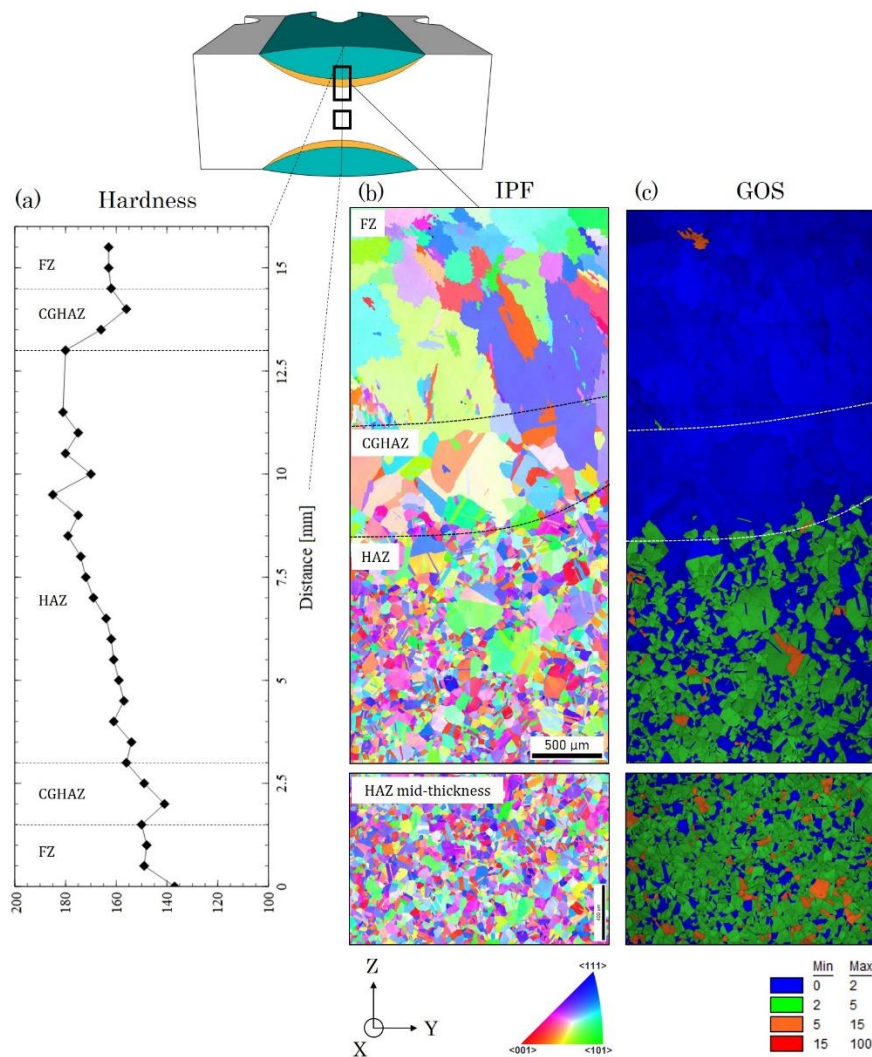


Figure 3: Microstructure of studied 316L(N) steel after welding: (a) HV1 Hardness profile along the Z-axis, (b) IPF (Inverse Pole Figure) of the weld zones and (c) GOS (Grain Orientation Spread) map of the FZ (Fusion Zone), the CGHAZ (Coarse Grain Heat Affected Zone), the HAZ (Heat Affected Zone) and mid-thickness HAZ. Analysis was performed with acquisition step of 3  $\mu\text{m}$ .

## 2) Mechanical characterization of weld zones

Mechanical tensile tests were performed with both welded and non-welded samples to evaluate the impact of welding on mechanical properties and further use the data to determine the parameters of the mechanical model presented in Section 2) **b) Estimation of residual stresses induced by compression**. The model was then used to perform numerical simulations of the compression test and compute residual stress and strain, as presented in Section 3) **Introduction of residual stress by compression**.

Tensile tests were carried out at room temperature using samples machined directly from the welded plate in both X and Y directions, allowing determining the properties of the different zones of the welded microstructure and thus better predict mechanical behavior during compression. A total of 30 tests were carried out, with 8 tests in the FZ, 4 in the CGHAZ and 18 in the HAZ because of the respective size of each zone. Isotropic behavior was observed in the (XY) plane for all regions. Yield strength was slightly higher for the HAZ than that in the as-received material, FZ and CGHAZ, in agreement with hardness measurements (Figure 3 (a)). However, the ultimate tensile strength in the HAZ was found to be similar to that in the as-received state, while it was lower in the FZ. It is worth noting that mechanical behavior of the CGHAZ was difficult to analyze reliably due to the low thickness of this region (from 0.55 to 1 mm), which is narrower than the tensile specimen thickness.

### 3) Controlled generation of residual stress by compression

SRC resistance of welded 316L(N) suggests that residual stresses induced by welding are not sufficiently high to lead to damage even after very long heat treatments. Hence, in this work additional residual stresses were introduced by compression at room temperature after the welding using CT samples directly machined from the welded plates, as illustrated in Figure 1. Nevertheless, residual stresses due to welding were taken into account during preliminary FEM simulations of the compression test considering four stress states after the welding: (i) a zero-stress state, (ii) uniform initial transverse (Y direction) residual stress field of 400 MPa, (iii) longitudinal (X direction) residual stress field of 400 MPa and finally (iv) both longitudinal residual stress fields. The non-zero stress scenarios were intentionally chosen as exaggerated cases since real values of residual stresses due to welding without filler metal and for a single pass are much lower and are more localized near the FZ. The comparison of computed post-compression principal residual stresses at the notch of the CT specimens for the four cases showed no differences in magnitude nor distribution. It was thus concluded that the compression entirely redistributes stresses at the notch of CT sample due to the high plastic straining in this area. Consequently, residual stresses induced by welding were not further taken into account.

Four compression loads were then applied for simulation, resulting in CMODs of 1.39, 1.73, 6.09 and 6.41 mm as obtained in experimental compression (Table 2). Force as function of CMOD measured during experimental compression loading are compared to those obtained from FEM computations in Figure 4. The results of FEM computations were found to be in very good agreement with experimental measurements for moderate final CMODs (1.39 and 1.73 mm) (Figure 4 (a)). A slight difference was observed for higher CMODs (6.09 and 6.41 mm), but similar behavior upon unloading for both numerical and experimental curves (Figure 4 (b)). The difference between computed and experimental curves can be related to the simplified computations hypothesis chosen for these simulations. Notably, the parameters of the Chaboche elastic-plastic model (Equations 1-4), which were adjusted only using the results of tensile tests, and the simplified mesh geometry describing the heterogeneous properties of the CT specimen, accounting only for the mechanical behavior of the FZ and the HAZ. Moreover, displacement limitations of the experimental extensometer could be the origin of such differences as well.

Maximum residual tensile stress and plastic strain values were found in the Y direction for all specimens, parallel to the loading direction (Figure 4 (c) and (d)). For specimens with highest CMODs of 6.09 and 6.41 mm the maximum principal residual stresses,  $\sigma_{yy}$ , predicted at half-thickness were 938 and 949 MPa, respectively (Figure 4 (e)). The SRC threshold of 740 MPa, suggested by Pommier [13], was thus reached for these compression conditions and the development of micro and macro cracks could be thus expected after a thermal treatment. According to the FEM simulations, the two high CMODs resulted in very similar residual stress and strain (Figure 4 (b)). They were therefore considered to have the same mechanical state before the heat treatment for further comparisons.

In the case of lower CMODs, 1.39 and 1.73 mm, the maximum residual stresses,  $\sigma_{yy}$ , predicted at half-thickness were 655 and 681 MPa, respectively (Figure 4 (e)). The lower pre-loaded levels applied to these specimens are not expected to lead to the formation of cracks. However, these preloads could allow the formation of GB cavities, requiring lower magnitudes of stress and strain. Such specimens would then allow better characterizing and understanding the SRC mechanism involving microstructure features.

Residual stress distributions showed that maximum values of stress were constrained near the notch in a  $300 \times 300 \mu\text{m}^2$  region (XY plane). As shown in Figure 4 (d) and (f), residual stress magnitude was not completely homogeneous throughout the specimen thickness (Z-axis). For the CMOD of 1.73 mm, a 400 MPa maximum of residual stress was predicted at the surface of the sample, against 681 MPa at mid-thickness. The difference is more pronounced for the highest CMODs, with a difference of 424 MPa between the surface and mid-thickness. These residual stress gradients were taken into account for all specimens for the analyses of damage in the different regions in order to avoid misinterpretations. Also, as it will be presented in **4) Analysis of SRC**, damage analyses were mainly performed between the FZ/CGHAZ boundary (near  $Z = 3.0$  mm) and the specimen mid-thickness, hence with a much lower difference in stress peaks. For the CMOD of 1.73 mm, difference in residual stress between FZ/CGHAZ boundary and mid-thickness was evaluated to be 98 MPa and that for the CMOD of 6.41 mm, was estimated to be 52 MPa.

Plastic strain showed a rapid decrease when moving from the notch along X axis (Figure 4 (e)). Higher plastic strains were found at the notch, with maximum values higher than 10% predicted for all specimens. According to Chabaud-Reytier [16], such pre-strain levels are favorable to SRC. It is worth noting that the maxima of stress and plastic strain are generally not coincident, especially for the higher CMODs with stress maximum shifting towards a distance of 200 to 300  $\mu\text{m}$  from the notch. The computed distribution and magnitudes of both stress and strain were found to be consistent with results described in the literature for similar compressions tests and material [13, 23].

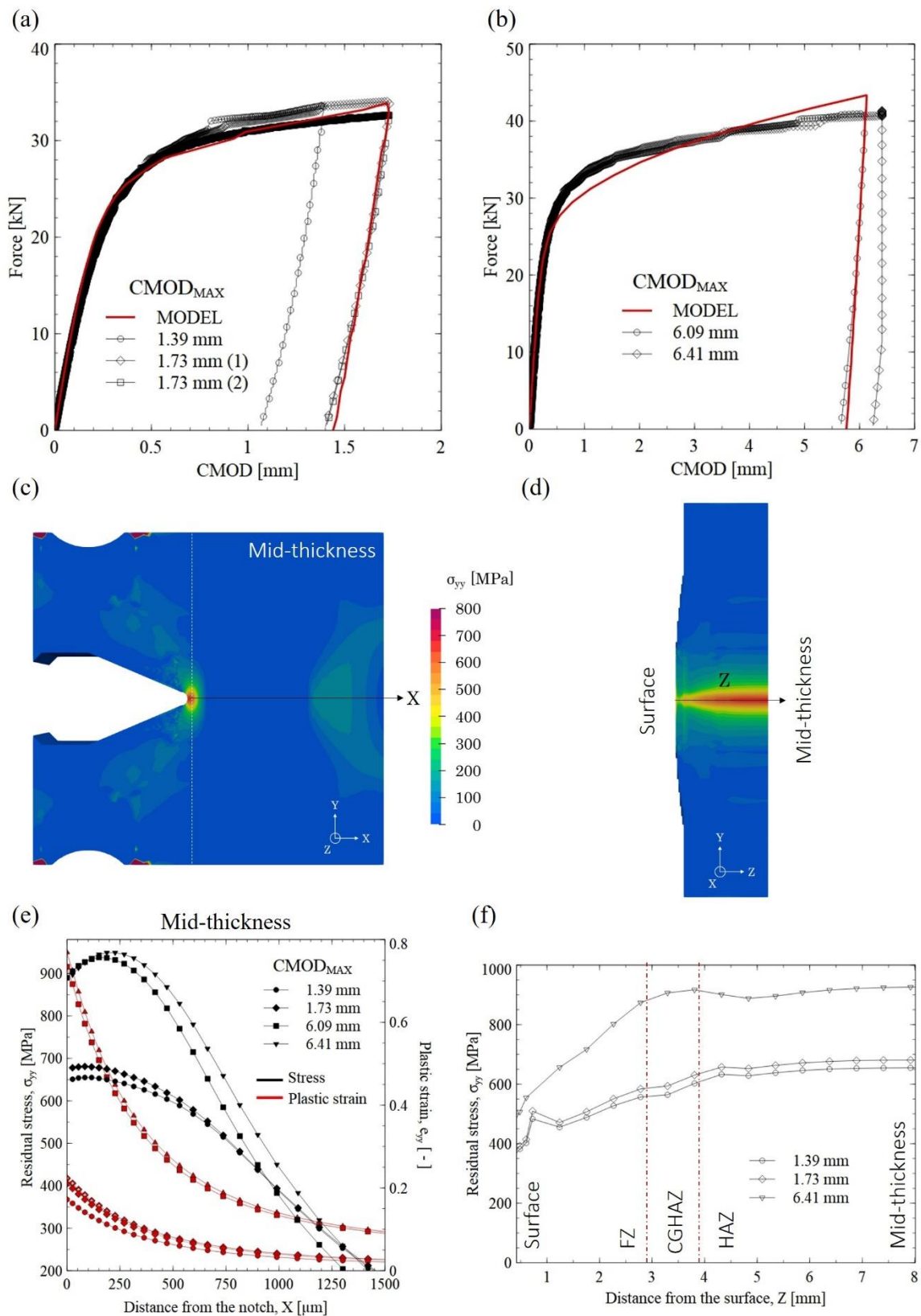


Figure 4: Experimental and simulated (MODEL) curves of force as function of CMOD (Crack Mouth Opening Displacement) in absolute value during compression of CT (Compact Tension) specimens machined from welded plate for (a) moderate CMOD and (b) high CMOD. (c) Computed  $\sigma_{yy}$  stress field for maximum CMOD of 1.73 mm after compression, at half-thickness of CT sample ( $z = 7.5$  mm) and (d) near the notch in the (YZ) plan. (e) Calculated residual stress,  $\sigma_{yy}$ , and plastic strain,  $e_{yy}$ , in X direction after compression at mid-thickness and (f) along thickness-direction at a distance  $X = 25$

$\mu\text{m}$  from the notch root. FZ stands for Fusion Zone, CGHAZ for Coarse Grain Heat affected Zone, and HAZ for Heat affected Zone.

#### 4) Analysis of stress relaxation cracking

After compression, the samples were heat treated at 575 °C for 580 and 1470 h (Table 2), allowing stress relaxation and thus aiming to trigger SRC. After the heat treatment, the samples were prepared for analyses with the SEM, according to the procedure described previously (Figure 2), and observations were carried out in different planes of the CT samples to analyze the features induced by stress relaxation close to the notch root.

After thermal treatment at 575 °C for 580 and 1470 h, SEM observations of the two as-welded specimens (without compression) did not reveal any damage, whether in the form of crack or cavities. This indicated that the residual stresses (lower than 400 MPa) and plastic strain (lower than 5%) induced by welding were not sufficient to cause SRC in the studied 316L(N) steel. The low susceptibility of this material to SRC confirmed the necessity to carry out an additional compression stage to enhance the driven forces triggering the nucleation of damage.

##### 1) Local damage study

Investigation of damage was carried out in the (YZ) and (XY) planes by SEM in the three weld zones (FZ, CGHAZ and HAZ) of specimens submitted to the same heat treatment, at 575 °C for 1470 h, but different compression loads: CMODs of 1.39, 1.73 and 6.41 mm. The influence of the welding microstructure, pre-compression magnitude, relaxation time and microstructural features on the initiation of damage are presented in the following. The nucleation sites and distribution of damage are also discussed.

- **Influence of the welding microstructure on SRC**

The specimen after pre-compression with CMOD of 1.73 mm further aged at 575 °C for 1470 h was chosen to analyze microstructural effects on damage. Damage in this specimen appeared mainly in the form of intergranular cavities, with only a single microcrack composed of coalesced cavities being observed at the FZ/CGHAZ interface, as detailed in Figure 5 (a). Figure 5 (b) shows an overview of the region within which cavities were observed by SEM for FZ, CGHAZ and HAZ. It can clearly be seen that the CGHAZ is the most damaged region where intergranular cavities have coalesced and led to a crack with a length of several hundreds of  $\mu\text{m}$ , Figure 5 (a). As it is shown on the IPF map given in Figure 5 (c), these cavities in the CGHAZ were situated on a GB that was oriented normal to the principal residual stresses (Y axis). There are cavities but no cracks observed in both the FZ and the HAZ, with the least apparent damage seen in the HAZ.

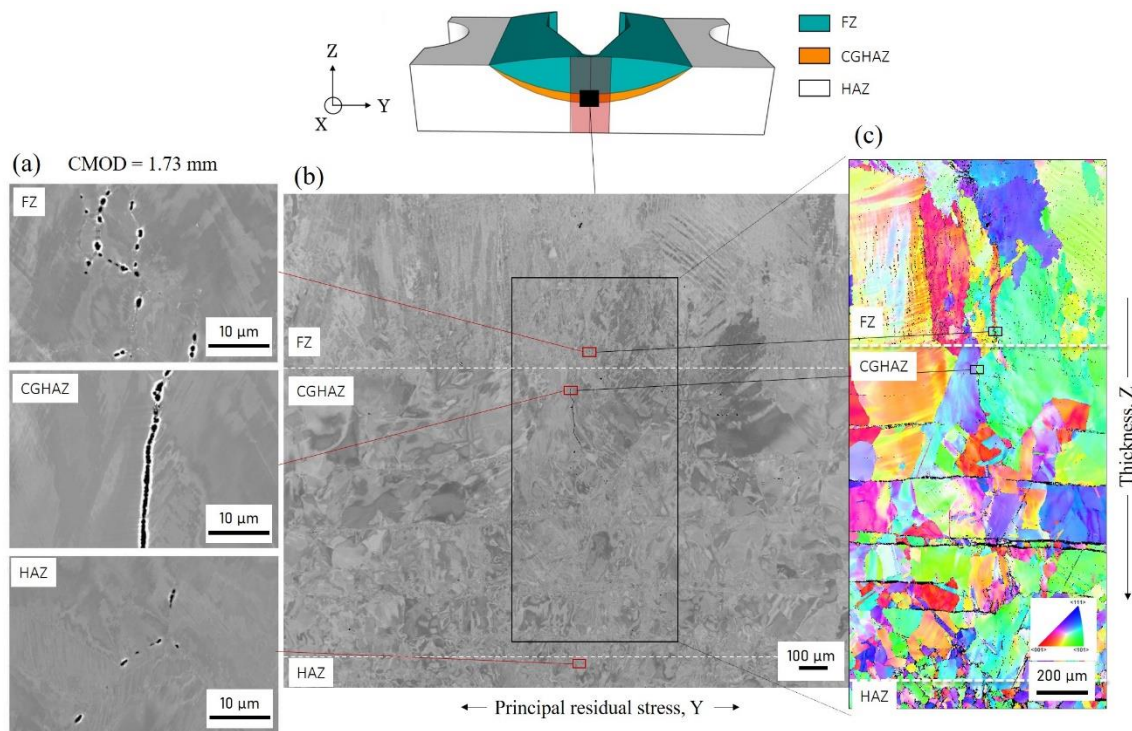


Figure 5: Observation of SRC (Stress Relaxation Cracking) in a CT (Compact Tension) specimen at a distance of 40  $\mu\text{m}$  from the notch root in the (YZ) plane. The specimen was pre-compressed to a maximum CMOD (Crack Mouth Opening Displacement) of 1.79 mm and further aged at 575  $^{\circ}\text{C}$  for 1470 h. (a) close-up SEM (Scanning Electron Microscope) images of damage observed in the region shown in (b), with the corresponding IPF (Inverse Pole Figure) map in (c). FZ stands for Fusion Zone, CGHAZ for Coarse Grain Heat affected Zone, and HAZ for Heat affected Zone.

#### • Cavity nucleation sites

SEM observations carried out on the different samples highlighted the preferential sites for cavity nucleation:

(i) at ferrite interfaces, mostly in the vermicular ferrite in the FZ, less frequently in the residual ferrite found in both the CGHAZ and the HAZ;

(ii) at intergranular precipitates in the three weld zones. Additional EBSD analyses allowed the identification of possible phases associated with these cavities (Figure 6), but also the effect of microstructural features on the presence of GB cavities.

EBSD results suggested that 30% of cavities in the FZ were formed on precipitates located at austenite GBs while 70% of cavities were found at vermicular ferrite and austenite interfaces but also within former vermicular ferrite grains partially transformed into regenerated austenite,  $\gamma_{\text{R}}$ ,  $\text{Cr}_{23}\text{C}_6$  carbides and  $\sigma$  phase during the heat treatment (Figure 6 (a)). These results are in agreement with observations of Vijayanand *et al.* [60] for creep damage in the FZ of a welded 316L(N) steel.

In this weld zone, the number of brittle precipitates in the decomposed vermicular ferrite and their size were higher than on the austenite GBs (Figure 6), which most likely favored the nucleation of cavities in these areas because of strain mismatch and stress concentration [60].

In the CGHAZ, cavities were mostly found to form on  $\text{Cr}_{23}\text{C}_6$  GB precipitates, as suggested by analysis shown in Figure 6 (b). SEM-BSE images and EDS (Energy Dispersive X-ray Spectroscopy) analyses of precipitates near cavities in these two regions also showed the presence of the smaller Mo-rich intermetallic phases (Figure 6 (e)), often identified in the literature as Laves phases [58, 61]. Less often, cavities were also observed in the partially decomposed residual ferrite areas (Figure 6 (d)). The fraction of cavities observed on the residual ferrite in this weld zone was generally less than 11%. Similarly to the CGHAZ, cavities observed in the HAZ were mostly located on intergranular  $\text{Cr}_{23}\text{C}_6$  precipitates

(Figure 6 (c)), and a few on the residual ferrite sites.  $\text{Cr}_{23}\text{C}_6$  precipitates in both the CGHAZ and the HAZ presented similar sizes, comprised between 200 and 500 nm. Number of precipitates per unit length of GB was also observed to be similar in these two zones.

EBSD analyses along with SEM images of cavities also suggested a majority of cavities were located at GBs with the plane which was transverse to the pre-compression axis and with GB misorientation angle comprised between 25 and 55°, in agreement with results of Pommier [13] for a similar steel.

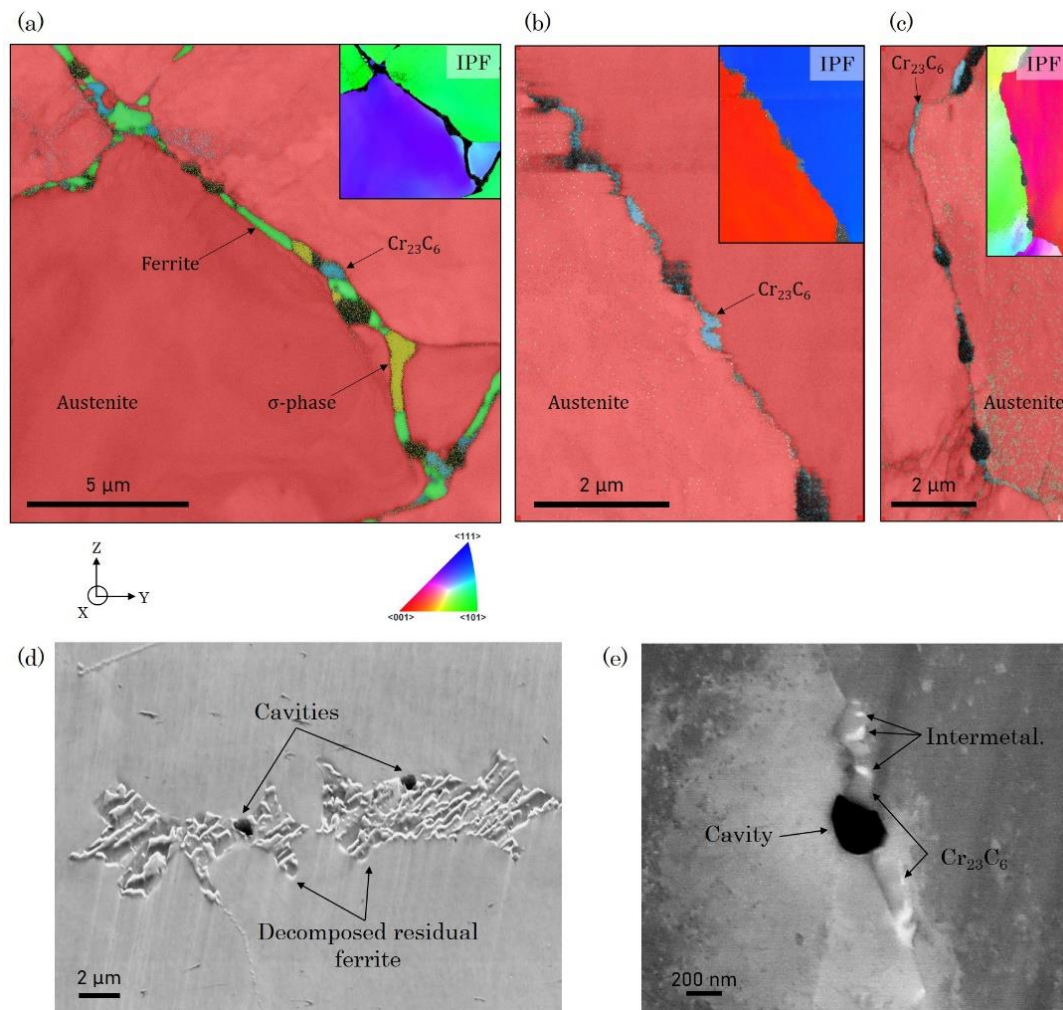


Figure 6: Sites of cavity nucleation by stress relaxation in (a) FZ (Fusion Zone), (b) CGHAZ (Coarse Grain Heat Affected Zone), (c) HAZ (Heat Affected Zone) and (d) residual ferrite observed in 316L(N) steel after welding, compression and heat treatment at 575 °C for 1470 h. (e) SEM (Scanning Electron Microscope) image of Mo-rich precipitates among GB (Grain Boundary)  $\text{Cr}_{23}\text{C}_6$  precipitates close to a cavity, observed in both the CGHAZ and HAZ. (a), (b) and (c) phase maps superposed with index quality maps acquired by EBSD (Electron Back Scatter Diffraction) with step sizes of 20, 15 and 20 nm, respectively. IPF (Inverse Pole Figure) maps of austenite are also given for grain distinction. Horizontal Y axis corresponds to the compression direction.

Therefore, SRC initiated by cavity nucleation in the 316L(N) in both the HAZ and CGHAZ is induced by the presence of GB precipitates, in agreement with literature results on non-welded 316L(N) [13]. To quantify the damage, cavity distribution after relaxation treatment was analyzed along both Z and Y directions; GOS averaged over the zones as a local measure related to the plastic strain was measured by EBSD analyses as well. GOS is sometimes used to estimate local deformation, as in the works of Carneiro *et al.* [62].

- **Damage and grain orientation spread for the three weld zones**

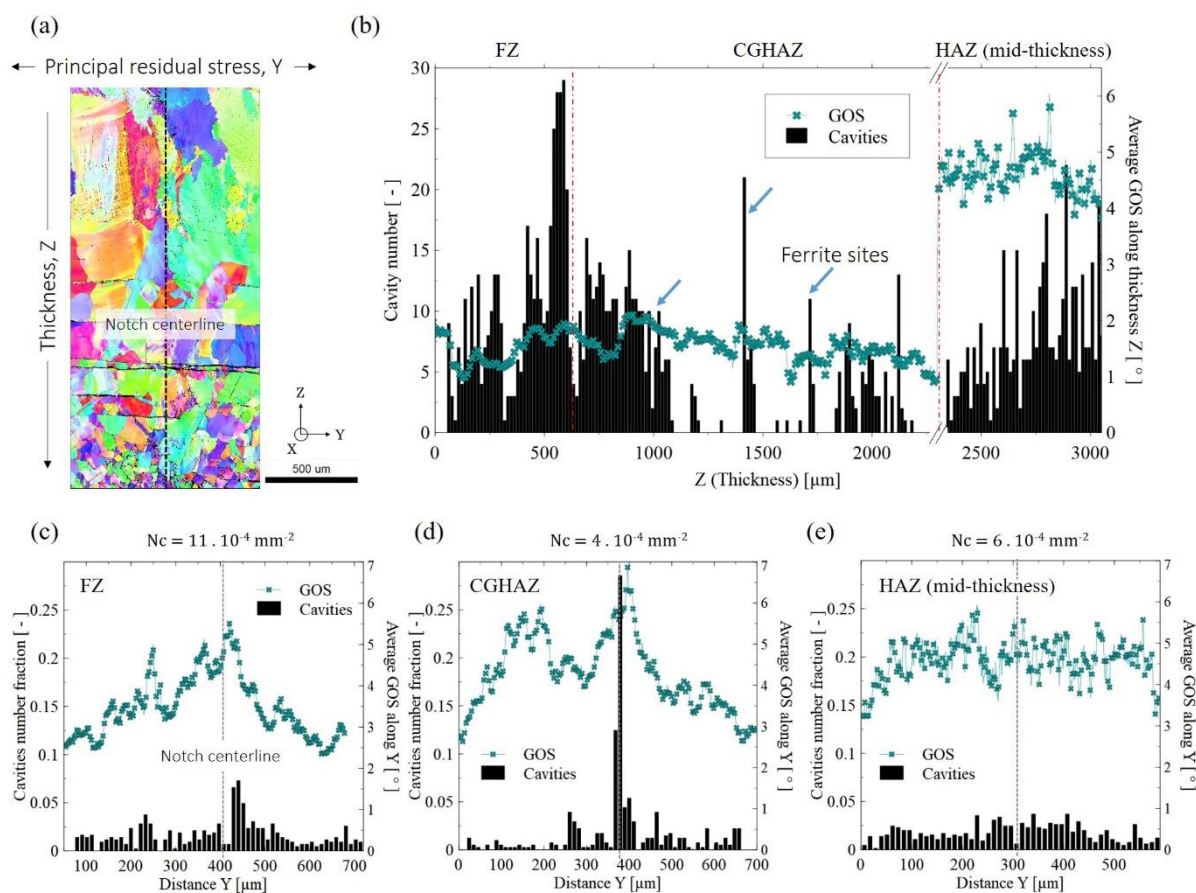


Figure 7: Comparison of cavity distribution in the FZ (near boundary with CGHAZ), CGHAZ and HAZ (at half thickness) after welding. The specimen was pre-compressed to a maximum CMOD (Crack Mouth Opening Displacement) of 1.79 mm and further aged at 575 °C for 1470 h. (a) IPF (Inverse Pole Figure) over IQ (Index Quality), (b) and (c)-(e) cavities and GOS (Grain Orientation Spread) distribution along the Z and Y axes, respectively. Nc indicates the cavity number per unit area for each zone. FZ stands for Fusion Zone, CGHAZ for Coarse Grain Heat affected Zone, and HAZ for Heat affected Zone.

The specimen pre-compressed to CMOD of 1.79 mm and further aged at 575 °C for 1470 h was selected to characterize the distribution of cavities over the zones affected by welding (Figure 7 (a)). Cavities analysis along CT sample thickness (Z axis) shown in Figure 7 (b) indicated a very heterogeneous distribution across three weld zones whose interfaces are represented by red dashed-dotted lines. According to FEM simulations presented in Figure 4 (f), a slight progressive increase of stress from the sample surface to the half-thickness should be expected. However, instead of progressive increase in cavity number from the surface towards mid-thickness, here the cavity distribution was found to be more complex with significant variations throughout the thickness. This indicates the significant role of the microstructure on damage.

The number of cavities increased in the FZ towards the FZ/CGHAZ boundary (along Z axis) where the highest cavity number was found. From there, a high number of cavities was found at the top of the CGHAZ, and almost no cavities in the center of the CGHAZ besides some in residual ferrite (indicated by blue arrow). A significant number of cavities was then observed again at the bottom of the CGHAZ. The number of cavities then progressively increased towards the mid-thickness in the HAZ, presenting a more homogeneous distribution of damage compared to the two other regions. The average GOS profile in the Z direction did not show a clear correlation with cavity distribution, with higher cavity number not apparently related to higher GOS values. GOS in the FZ increased slightly towards the

FZ/CGHAZ boundary, with similar magnitude to that in the CGHAZ. In the CGHAZ, the GOS profile appeared to decrease towards the bottom of the zone. As expected from the computed plastic strain evolution through thickness Z, GOS values at mid-thickness in the HAZ were higher than in the two other regions.

Increase in cavity number towards the FZ/CGHAZ boundary observed in the FZ is most probably due to the increase in stress and strain towards mid-thickness, as suggested by the FEM computations (Figure 4 (f)), but also to the different microstructure observed within the FZ. Mostly equiaxed grains were present near the FZ surface, while larger columnar grains (with grain size larger than 200  $\mu\text{m}$ ) were observed near the FZ/CGHAZ boundary (Figure 3). For the FZ, most of the cavities were located on the partially decomposed vermicular ferrite: only 29% of the 456 identified cavities in this region were located at austenite GBs against 71% on the ferrite. This can be related to the lower austenite GB density near the FZ/CGHAZ boundary. As a result, the available surface for cavities nucleation at austenite GBs is significantly lower than the ferrite/austenite interface. Damage in the CGHAZ was concentrated on a few grain boundaries, especially near the FZ/CGHAZ boundary with more than 54% of the cavities, here being coalesced cavities, located on a single grain boundary. The more homogeneous distribution of cavities in the HAZ was most probably favored by a higher density of GBs observed in this zone.

Cavity distribution and average GOS profile were also computed as a function of the Y (compression) direction (Figures 7 (c) to (e)) over the whole respective zones, to better reveal the characteristics of each zone. In these three figures, the notch centerline, which corresponds to the maximum of computed stress and strain near the notch, was indicated by grey dashed lines. Damage was plotted as cavity number fraction to better compare the three zones in terms of distribution heterogeneities. According to such an analysis, in the FZ cavities were relatively homogeneously distributed over the Y direction, but with an increase towards the notch centerline as shown by Figure 7 (c), consistent with expected higher magnitudes of both stress and strain towards the notch. The average GOS profile in the FZ showed a very good correlation with cavity distribution, with coincident peaks and global evolution over the whole zone. The CGHAZ again presented the most heterogeneous cavity distribution when compared to the two other weld zones, illustrated by the highest peak of cavity number (Figure 7 (d)), here being coalesced cavities forming a crack. The average GOS profile in the CGHAZ showed a good correlation with cavity distribution for  $Y > 250 \mu\text{m}$ , with coincident peaks and global evolution. However, for  $Y < 250 \mu\text{m}$ , high magnitudes of GOS were observed while very few cavities were found. This revealed a very particular behavior of the CGHAZ.

As for the analysis in the Z direction, cavity distribution in the HAZ integrated over the Y direction was the most homogeneous (Figure 7 (e)). Cavity distribution was consistent with the GOS profile, with no significant peaks in cavity number or GOS as compared to the two other zones.

The total cavity number per unit area was also computed for each region, with  $11 \times 10^{-4}$ ,  $4 \times 10^{-4}$  and  $6 \times 10^{-4} \text{ mm}^{-2}$  in the FZ, CGHAZ and HAZ, respectively. This showed the FZ was the most affected zone by cavities, followed by the HAZ and finally the CGHAZ. This is in agreement with the observations carried out in the Z direction discussed previously. However, the CGHAZ was determined to be the most prone to SRC as it contained the only crack found in the specimen.

The comparison of average GOS with cavity distribution showed that the heterogeneous distribution of damage in the FZ and CGHAZ was most probably, at least partially, related to a heterogeneous strain in these two regions. Similarly, the homogeneous distribution of damage in the HAZ was related to a homogeneous strain over the whole region.

Cavity distributions were also characterized in a homogeneous microstructure (in terms of grain size and morphology), carrying out the analyses in the (XY) plane at the notch of the same specimen,

pre-compressed to CMOD of 1.73 mm (Figure 8 (a)). Cavity distribution followed, to some extent, the evolution of the plastic strain and residual stresses estimated by FEM simulations (Figure 8 (b)).

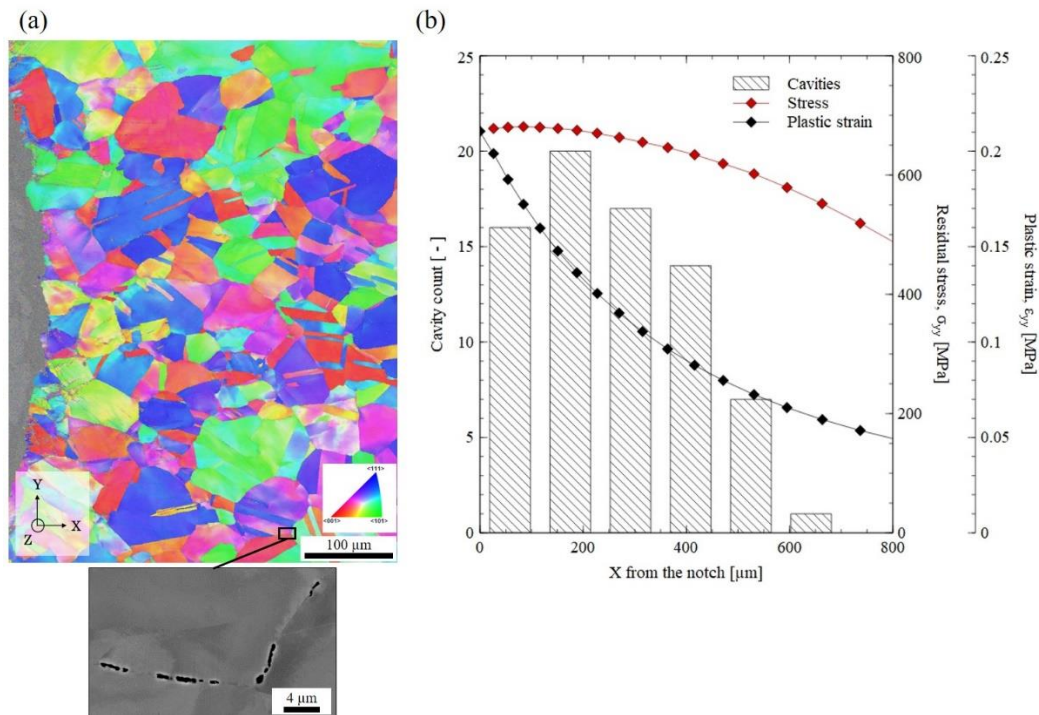


Figure 8: Analysis of damage in the HAZ (Heat Affected Zone) of welded 316L(N) steel after pre-compression to a CMOD (Crack Mouth Opening Displacement) of 1.73 mm and further heat treated at 575 °C for 1470 h: (a) IPF of the region of interest along Z axis (step = 550 nm) with a close-up of GB (Grain Boundary) and (b) distribution of cavities as function of the distance X from the notch compared to the computed post-compression residual stress  $\sigma_{yy}$  and plastic strain  $\epsilon_{yy}$  (in absolute value).

#### • Influence of pre-compression level on SRC

Figure 9 shows SEM micrographs of typical intergranular damage found in each zone of specimens pre-compressed to CMODs of 1.39, 1.73 and 6.41 mm, and submitted to the same heat treatment at 575 °C for 1470 h. Figure 10 compares the damage distribution and number of cavities for each specimen. The increase in CMOD highly increased the damage level, with specimens of higher CMOD presenting higher crack number. Moreover, as stated previously for the sample with CMOD of 1.73 mm, the FZ and HAZ presented more homogenous damage distribution, while in CGHAZ damage was concentrated on few grain boundaries leading to cracks by cavity coalescence. Even though the total number of cavities was observed to be higher in the HAZ than in the CGHAZ, CMODs of 1.39 and 1.73 mm did not result in the observation of any crack in the HAZ. Cracks in the HAZ were only observed for the highest CMOD of 6.41 mm, with only a few of them propagating along multiple GBs (Figure 10).

Correlations between damage analyses in both (XY) and (YZ) planes and the FEM computations (Figure 4) allowed the estimation of stress and strain thresholds required to induce damage in the different weld zones (Table 4). The threshold for cavity nucleation is first discussed with analyses of less pre-compressed specimens, and the threshold for cracking is then discussed with analyses of highly pre-compressed specimens.

For the less pre-compressed specimen (CMOD of 1.39 mm), first cavities were observed near the FZ surface in the (YZ) plane (cannot be seen in the figures), which corresponds to calculated stress and

strain of 490 MPa and 9%, respectively. For this same CMOD, the CGHAZ was the least damaged zone, with several isolated cavities located exclusively on a few grain boundaries (Figure 10 (a)). Predicted stress and plastic strain thresholds for cavity nucleation were 590 MPa and 15%, respectively. In the HAZ, cavities were observed at stress and strain levels higher than 650 MPa and 17%, respectively. These values represent the upper limit for cavity nucleation in the HAZ and further analyses were thus required. Investigation of damage was then carried out in the (XY) plane for CMOD of 1.73 mm in the HAZ, allowed the determination of stress and strain threshold in another plane (Figure 8). The characterization in this plan was facilitated by the homogeneous microstructure, as the (XY) plan is transverse to the microstructure evolution induced by welding (Z direction). The comparison of cavity number with simulation results obtained by FEM (Figure 8 (b)) suggested that cavities in the HAZ appeared above 460 MPa of residual stress and 5% of plastic strain. This is in agreement with results obtained previously for the (YZ) plane and data reported by Chabaud-Reytier [16] who suggested a pre-strain threshold between 5 and 10% to induce SRC in the 321 steel.

Similarly, thresholds for cracking were then investigated for the three zones, with analyses of the highly pre-compressed specimens. Micro- and macrocracks in the FZ were observed only for the most pre-compressed specimen (Figure 10), corresponding to stress and strain thresholds around 900 MPa and 52%, respectively, which corresponded to extreme conditions as compared to those in industrial applications. In the HAZ, cracks were only observed in the specimen compressed to a CMOD of 6.41 mm, corresponding to stress magnitudes comprised between 680 and 930 MPa and 21 and 74% of plastic strain. As for cavity nucleation threshold in the HAZ, cracking in the HAZ required additional analyses to estimate more precisely threshold magnitudes. Hence, the specimen compressed to a CMOD of 6.41 mm and heat treated at 575 °C for 1470 h was further analyzed in the (XY) plane at half thickness. The first cracks were observed at a distance of 426  $\mu\text{m}$  from the notch, which corresponds to calculated stress and strain of 890 MPa and 30%, respectively. This is consistent with first results obtained in the (YZ) plane (Table 4), but higher than the SRC thresholds of 740  $\pm$  40 MPa stress and 20-30% strain suggested by Pommier [13] for a strained 316L(N) with similar composition and mechanical properties. This difference could come from the composition of the steel or pre-strain level as mentioned in the introduction. In the CGHAZ, the first crack was detected in the specimen compressed to a CMOD of 1.73 mm. For this specimen, the stress and strain crack threshold in this zone was estimated to be 600 MPa and 18%, respectively. This low value of cracking threshold can be related to the particularly favorable microstructure: a long GB ( $> 200 \mu\text{m}$ ) located beneath the FZ/CGHAZ boundary oriented in almost transverse direction to the residual tensile stress Y axis. While this makes the estimation of SRC threshold in the CGHAZ difficult, due to potential microstructure variations from one sample to another, it can be suggested however that a GB particularly favorable to SRC in the CGHAZ can be highly detrimental for damage development. Such an effect is less pronounced in other welding regions since more GBs are found there and they can accumulate more cavities in the same volume (detailed in **5 Discussion**).

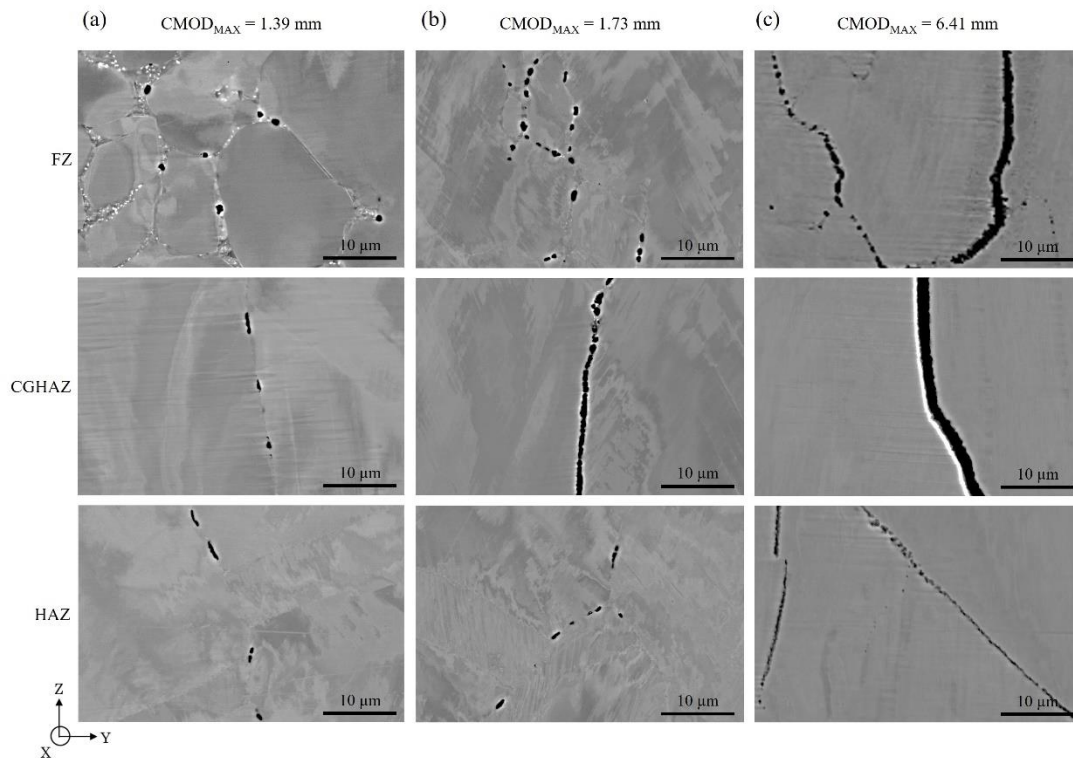


Figure 9: Cavities and cracks observed in 316L(N) steel after pre-compression with different CMOD (Crack Mouth Opening Displacement) and further heat treatment at 575 °C for 1470 h: (a) 1.39, (b) 1.73 and (c) 6.41 mm (BSE-Back Scattered Electrons image from SEM-Scanning Electron Microscope analysis). Residual stress direction corresponds to the Y axis. Z axis crosses the CT (Compact Tension) sample thickness. FZ stands for Fusion Zone, CGHAZ for Coarse Grain Heat affected Zone, and HAZ for Heat affected Zone.

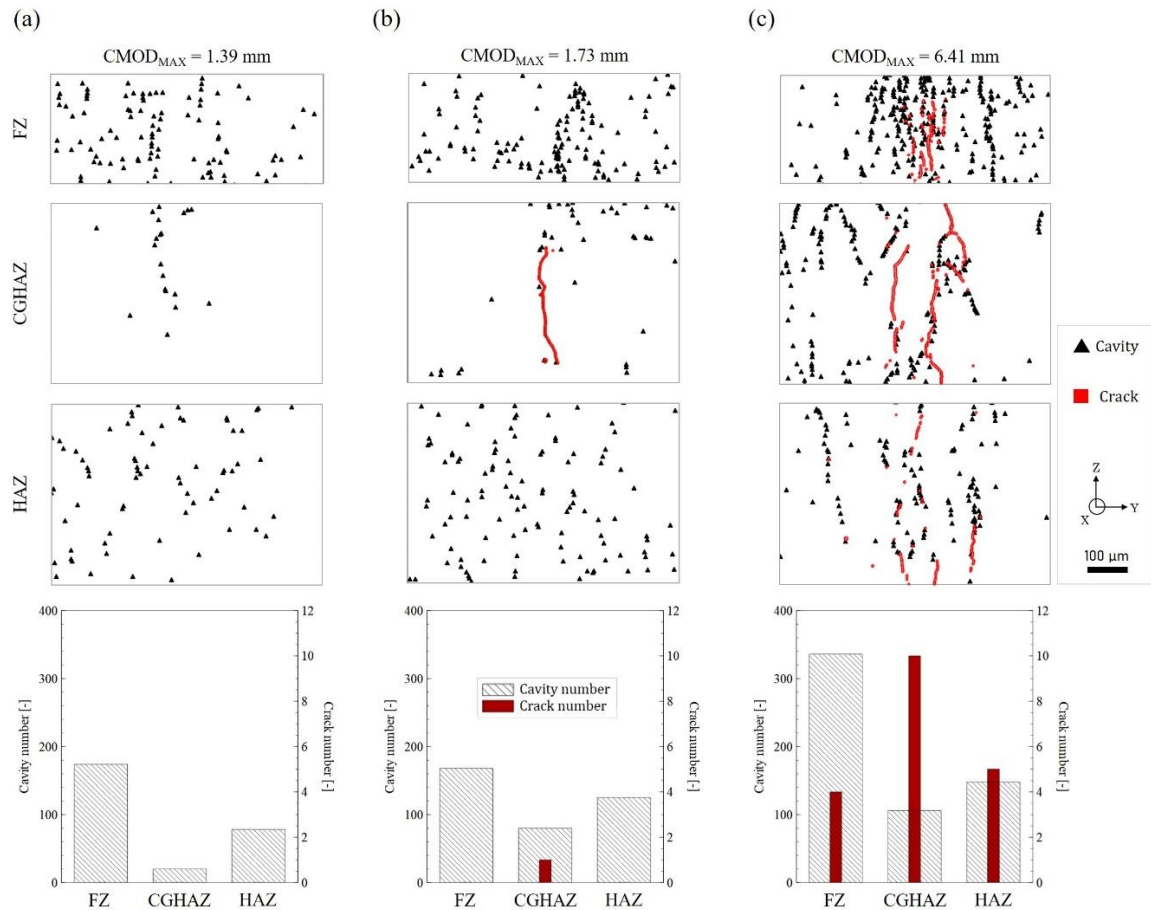


Figure 10: Comparison of stress relaxation damage observed in the FZ (near boundary with CGHAZ), CGHAZ and HAZ (at half thickness) of 316L(N) steel after welding, pre-compression with different maximum CMOD (Crack Mouth Opening Displacement): (a) 1.39 mm, (b) 1.79 mm and (c) 6.41 mm and further heat-treated at 575 °C for 1470 h. FZ stands for Fusion Zone, CGHAZ for Coarse Grain Heat affected Zone, and HAZ for Heat affected Zone.

Table 4: Estimation of stress relaxation cavity nucleation and macro cracking thresholds for each region of the welded microstructure for relaxations conducted at 575 °C for 1470 h determined from analyses and FEM (Finite Element Method) simulation results in the (YZ) and (XY) planes.  $\delta$  stands for ferrite and  $\gamma$  for austenite. FZ stands for Fusion Zone, CGHAZ for Coarse Grain Heat affected Zone, and HAZ for Heat affected Zone.

| Weld region         | FZ                                   |                      | CGHAZ                |                      | HAZ                  |                      |
|---------------------|--------------------------------------|----------------------|----------------------|----------------------|----------------------|----------------------|
|                     | Cavities                             | Cracks               | Cavities             | Cracks               | Cavities             | Cracks               |
| Damage location     | $\delta, \gamma, \sigma, Cr_{23}C_6$ | $\gamma, Cr_{23}C_6$ |
| $\sigma_{yy}$ [MPa] | 490                                  | < 900                | 580                  | 600                  | 460                  | 890                  |
| $e_{yy}$ [%]        | 9                                    | < 52                 | 15                   | 18                   | 5                    | 30                   |

• **Influence of relaxation time on SRC**

Figure 11 illustrates the influence of post compression relaxation time on the nature, distribution and magnitude of damage. Local damage was compared for welded 316L(N) steel after compression with similar CMODs of 6.09 and 6.41 mm and further heat treatment at 575 °C for 580 and 1470 h, respectively. Globally, damage increased in all three welding zones with increase in relaxation time.

In the FZ, damage mostly consisted of cavities and a few small micro-cracks (several coalesced cavities) near the FZ/CGHAZ boundary after 580 h. After 1470 h of relaxation, the number of damaged GBs and number of cavities largely increased. This resulted in a broader damaged area and in more severe damage per boundary, which is manifested by a higher number of micro cracks (Figure 11). Analyzing the binarized SEM images of damaged FZ for both relaxation durations, this increase in damage was evaluated as an increase in surface damage by 90%.

In the CGHAZ, macro-cracks were already observed after 580 h of relaxation but only few GBs were affected. After 1470 h, numerous grain boundaries showed micro and macro-cracks (Figure 11). Analysis of binarized images revealed an increase of 120 % of surface damage in this zone when the relaxation time was increased to 1470 h.

In the HAZ, for shorter relaxation time, only few micro-cracks were observed, in addition to many cavities similarly to the FZ. After 1470 h, more grain boundaries were damaged. The number and length of micro-cracks also increased leading to surface damage increase by 80 %.

The investigation of damage evolution as function of relaxation time revealed that macro-cracks appeared quicker in the CGHAZ than in the FZ or HAZ. Even though cracks appeared in all three regions after 1470 h, SRC first occurred in the CGHAZ. Also, computation of surface damage evolution for the three zones showed that the increase in damage as a function of relaxation time was the most severe in the CGHAZ, followed by the FZ and finally the HAZ. It is probable that the steeper increase in damage in the CGHAZ is due to the presence of cracks for the shortest relaxation time, favoring the nucleation and growth of damage.

Overall, these results confirmed that the propensity to crack formation was higher in the CGHAZ than in the other regions, in agreement with results of the literature [22, 24, 25].

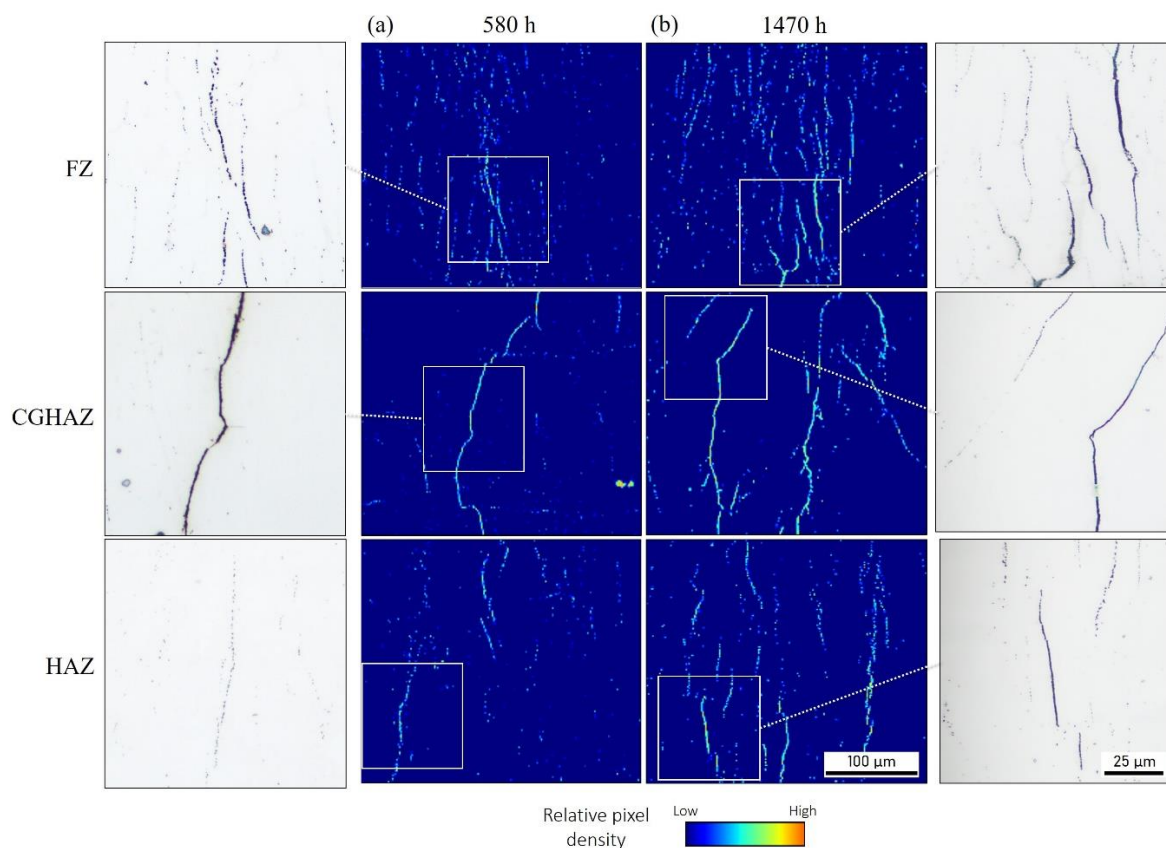


Figure 11: Effect of relaxation time for heat treatments carried out at 575 °C for (a) 580 h and (b) 1470 h after welding and compression of 316L(N) steel on damage in the FZ (near boundary with CGHAZ), CGHAZ and HAZ (at half thickness).

*Pixel density images (second and third column), computed from the local number of black pixels per unit area (see Material and Methods section). It illustrates the presence of cavities, micro and macro-cracks shown in associated optical microscopy images (first and fourth column). CMOD (Crack Mouth Opening Displacement) was about 6 mm for both specimens. FZ stands for Fusion Zone, CGHAZ for Coarse Grain Heat affected Zone, and HAZ for Heat affected Zone.*

### 3) SRC sensitivity of the CGHAZ

The results obtained from the observations carried out for pre-compression with different CMODs showed that the CGHAZ is more susceptible to SRC than the other regions affected by welding when exposed to similar or even slightly lower levels of residual stresses. As mentioned earlier, the residual stresses induced by welding were erased by the pre-compression and thus can be neglected when analyzing SRC phenomenon of welded and further compressed steel, as discussed in **3) Introduction of residual stress by compression**. The analyses allowed a better understanding of SRC in service industrial conditions where the damage was found to mostly initiate in the CGHAZ [2, 3, 20, 22, 25-27, 30, 36-39]. This proved the sensitivity of the zones affected by welding is not only due to high levels of residual stresses and strain, but is also microstructure dependent.

While several microstructural features detrimental for SRC were identified in the present study, such as the GB misorientation angle, the GB orientation to the direction of the principal residual stress, none of them could explain the higher sensitivity of the CGHAZ to SRC. It might be supposed thus that the high susceptibility of CGHAZ to SRC is mainly due to the overall large grain size in this zone and the absence of vermicular ferrite.

In this study, the grain size in the HAZ was shown to have locally no effect on GB cavities nucleation, as the grains in the HAZ which were larger than the average of the zone were not associated to higher number of cavities. The average grain size of an entire zone, rather than the local grain size, thus appeared to be the most probable factor explaining the sensitivity of the CGHAZ.

In order to verify this hypothesis, EBSD analyses of the section of the as-welded state were carried out (Figure 12). The total austenite GB length per unit area was measured to be lower in the CGHAZ than in both the FZ and the HAZ (Figure 12 (b)), impacting the plastic strain accommodation, and resulting in less free surface for cavity nucleation [8, 9, 25, 63]. Unlike in the FZ, cavities in the CGHAZ can only nucleate on austenite GB, besides from a few residual ferrite sites. This gives the CGHAZ even less possibility to homogeneously distribute damage. These results indicate that the microstructure is responsible for the lower SRC resistance of the CGHAZ.

While the authors also generally suggest that an increase in grain size leads to a decrease of grain boundary surface available for precipitation, an increase in precipitates number per boundary was not observed in the CGHAZ for the studied 316L(N) steel. However, the fraction of austenite GBs with misorientation angle between 25 and 55°, which were observed here to be the most favorable for cavity nucleation, was lower in CGHAZ than in the FZ, and similar to that in the HAZ (Figure 12 (c)). This is due to the fact that the fraction of 60° (111) annealing twin boundaries is higher in the HAZ and CGHAZ than in the FZ. Given the low energy of the (111) twin boundaries, no cavities were observed on these twin boundaries [13]. This again leads to the reduction in the number of potential sites for cavity initiation, resulting inevitably in a concentration of damage on the few sites available. At a mild state of damage, cavities will nucleate on a few GBs leading thus to a higher number of cavities per damaged boundary than in the other regions (Figure 9 (a)). At this state, damage localization is not yet an issue. However, an increase in pre-compression (i.e. CMOD) and/or relaxation time will result in an increase in cavity number on the few damaged GBs already presenting a high cavity density. Because of that, the coalescence of cavities and further development of cracks is much quicker in the CGHAZ (Figure 9 (b)). The lower GB density in the CGHAZ and longer GBs also favors the propagation of damage,

since triple points can act as obstacles [17]. This would then result in much longer intergranular cracks, as observed in the damaged specimens (Figure 10 (c)).

Additionally, it was shown through the GOS maps that the CGHAZ presented the most heterogeneous distribution of plastic strain contributing to stress localization and hence damage localization. TEM analyses also showed accumulation of dislocations tangles together with precipitates at GB areas, as illustrated in Figure 13. These two factors are known to facilitate cavity nucleation and further cracking [17]. It might be an explanation for decrease of SRC resistance of steels with increase in grain size [7, 35].

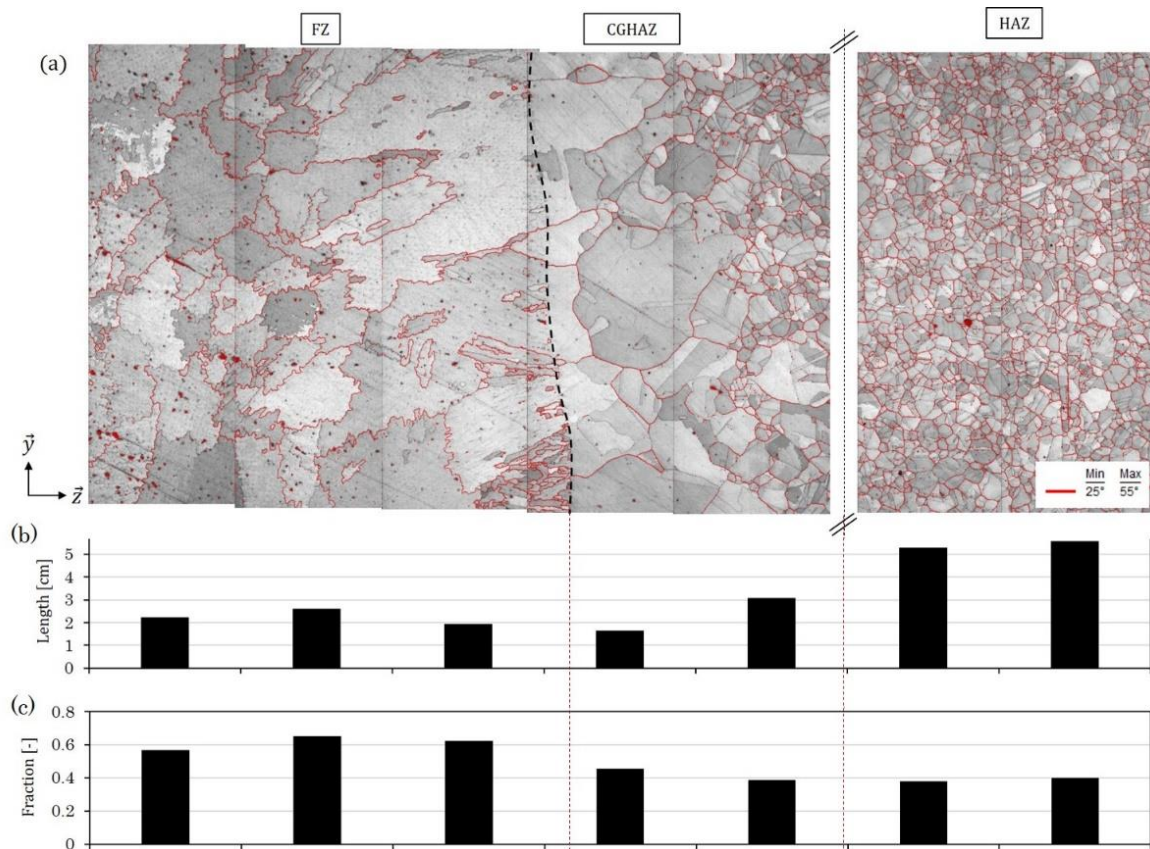


Figure 12: Austenite GB misorientation angle and length across the microstructure in as-welded state of 316L(N) steel: (a) GBs (in red) with misorientation angle between 25 and 55° over the quality index map, (b) GB fraction with misorientation angle between 25 and 55° and (c) total GB length fraction with misorientation angle between 25 and 55°. GB stands for Grain Boundary. FZ stands for Fusion Zone, CGHAZ for Coarse Grain Heat affected Zone, and HAZ for Heat affected Zone.

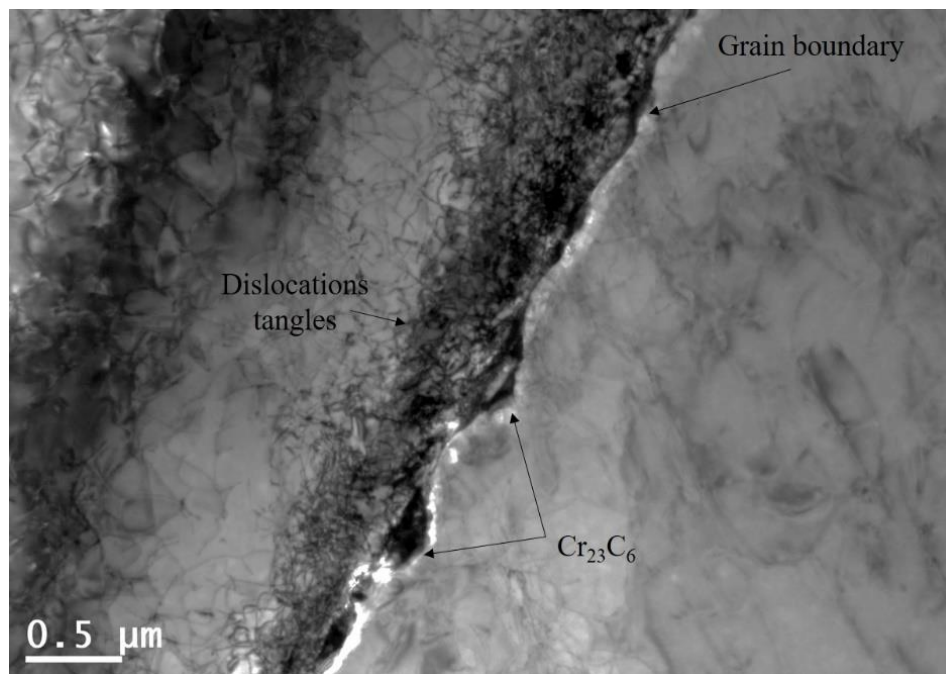


Figure 13: TEM (Transmission Electron Microscope) bright field image of dislocations tangles and  $Cr_{23}C_6$  precipitates at a damaged grain boundary in the CGHAZ (Coarse Grain Heat Affected Zone) of a specimen analyzed in the (YZ) plan after welding, pre-compression to a CMOD (Crack Mouth Opening Displacement) of 1.73 mm and further heat treatment at 575 °C for 1470 h.

## 5) Conclusions

A specific experimental procedure has been developed to induce SRC in a welded 316L(N) steel, known for its high resistance to SRC. After the welding without filler metal of a 316L(N) thick plate, CT-like specimens were machined from the plate and further compressed to generate controlled levels of residual stresses, theoretically sufficient to induce SRC phenomena. Both as welded and pre-compressed welded samples were further subjected to relaxation treatment at 575 °C for 580 and 1470 h. Analysis carried out on as welded samples without pre-compression revealed no damage following relaxation.

Damage induced by stress relaxation could be observed in pre-compressed welded CT specimens in the form of intergranular cavities, micro and macro cracks associated to precipitated secondary phases in agreement with the results available in the literature. The CGHAZ was most prone to SRC as most of the cracks were formed in this zone, with estimated thresholds of 600 MPa and 18% of plastic strain. These values are significantly higher than those induced by typical industrial GTAW multipass welding of 400 MPa and 5% [17], respectively.

For the first time, GB cavity nucleation was quantitatively correlated to local plastic strain, estimated with the measurement of grains crystallographic lattice distortions by the grain orientation spread (GOS) method using EBSD analyses. These analyses suggested a heterogeneous distribution of strain in both the FZ and the CGHAZ, but a homogeneous distribution of strain in the HAZ, consistent with observed cavity distribution. While the nucleation of cavities was found for lower stress and strain in the FZ than in the HAZ and CGHAZ, cracks appeared for lower levels of stress and strain in the CGHAZ as compared to the HAZ and the FZ. The high sensitivity to SRC of the CGHAZ was then attributed to highly heterogeneous distribution of both plastic strain and damage in this weld area, leading to cavity nucleation on the few available GBs. Higher density of cavities at lesser GBs resulted in easier cavity nucleation, growth and coalescence and facilitated crack initiation in CGHAZ.

### Data availability

Data will be made available on request.

### Acknowledges

The authors gratefully acknowledge the support of the CEA research project MATNA, related to the Generation IV program.

### Conflict of interest

The authors declare no conflict of interest.

### References

- [1] F. Dalle, M. Blat-Yrieix, S. Dubiez-Le Goff, C. Cabet and P. Dubuisson: *Structural Materials for Generation IV Nuclear Reactors*, Woodhead Publishing, 2017, pp. 595-633.
- [2] J.F Lancaster: *Handbook of Structural Welding: Processes, Materials and Methods Used in the Welding of Major Structures, Pipelines, and Process Plant*, Elsevier, 1997.
- [3] R. Loots: *Susceptibility of Service Exposed Creep Resistant Materials to Reheat Cracking During Repair Welding* (Doctoral dissertation, University of Pretoria), 2006.
- [4] Van Wortel, H.: *Control of Relaxation Cracking in Austenitic High Temperature Components*. In *NACE CORROSION*, March 2007, pp. NACE-07423.
- [5] L.E. Shoemaker, G.D. Smith, B.A. Baker, and J.M. Poole: *Fabricating nickel alloys to avoid stress relaxation cracking*. In *NACE CORROSION*, March 2007, pp. NACE-07421.
- [6] E. Barbareschi, P. Guarnone, A. Giostra, M. Zappaterra: *Materials Science and Technology*, 2009.
- [7] F. Dupoirion: *Corrosion in oil and gas industries high temperature working group: Workshop on relaxation cracking of stainless steels*, In *EUROCORR*, 2010.
- [8] M. Hussain, A. Hussain, and I. Hussain: *J. Failure Anal. Prev.*, 2018, vol. 18(4), pp. 733-758.
- [9] *Damage mechanisms affecting fixed equipment in the refining industry*, American Petroleum Institute (API), 2019.
- [10] R.M. Curran, and A. W. Rankin: *Trans. Am. Soc. Mech. Eng.*, 1957, vol. 79(6), pp. 1398-1409.
- [11] R.W. Emerson: *Res. Suppl. Weld. J.*, 1957, pp. 89-104.
- [12] R. N. Younger and R. G. Baker: *J. Iron Steel Inst.*, 1960, vol. 196, p. 1S8.
- [13] H. Pommier, E. P. Busso, T. F. Morgeneyer, A. Pineau: *Acta Mater.*, 2016, vol. 103, pp. 893-908.
- [14] B. Weiss, and R. Stickler: *Metall. Mater. Trans. B*, 1972, vol. 3, pp. 851-866.
- [15] A.S. Grot and J. E. Spruiell: *Metall. Trans. A*, 1975, vol. 6, pp. 2023-2030.
- [16] M. Chabaud-Reytier: *Étude de la fissuration différée par relaxation d'un acier inoxydable austénitique stabilisé au titane*, Lille thèses, 1999.
- [17] Q. Auzoux: *Fissuration en relaxation des aciers inoxydables austénitiques - Influence de l'écroûissage sur l'endommagement intergranulaire*. Doctoral dissertation, École Nationale Supérieure des Mines de Paris, 2004.
- [18] R.N. Younger, R. Baker and D. Haddrill: *J. Iron Steel Inst*, 1963, vol. 201(8), p. 693.
- [19] Y. Ito and M. Nakanishi: *J. Japan Weld. Soc.*, 1971, vol. 40, pp. 1261-1266.
- [20] C.D. Lundin and S. Mohammed: *Effect of welding conditions on transformation and properties of heat-affected zones in LWR (light-water reactor) vessel steels*, United States, 1990.
- [21] R. Unnikrishnan, S. M. Northover, H. Jazaeri and P. J. Bouchard: *Procedia Struct. Integr.*, 2016, vol. 2, pp. 3501-3507.

- [22] A. Dhooge, R.E. Dolby, J. Sebillé, R. Steinmetz and A.G. Vinckier: *Int. J. Press. Vessels Piping*, 1978, vol. 6(5), pp. 329-409.
- [23] M. Turski, P.J. Bouchard, A. Steuwer, P.J. Withers: *Acta Mater.*, 2008, vol. 6, pp. 3598-3612.
- [24] J. Lancaster, *Steel congress, Steel in the Chemical Industry*, 9-11.7, 1968.
- [25] N. Bailey: 6 - Reheat cracking. In *Weldability of Ferritic Steels*, edited by Norman Bailey, Woodhead Publishing Series in Welding and Other Joining Technologies, Woodhead Publishing, 1994, pp. 170-179.
- [26] L.-G. Liljestrånd, M. Aucouturier, G. Östberg, P. Lindhagen: *J. Nucl. Mater.*, 1978, vol. 75(1), pp. 52-67.
- [27] S. Soundararajan: *Stress Relaxation Cracking of TP 347H SS Flange Weld Joints on Reactor Charge Heater Manifold in Propane De-Hydrogenation Unit*, In *EUROCORR*, 2019.
- [28] Y. Cêtre: *La corrosion dans l'industrie chimique: Enjeux-Impact*, EDP Sciences, 2021.
- [29] O. Hellstroem, *Steel congress, Steel in the Chemical Industry*, Luxembourg 9-11.7, 1968.
- [30] D.A. Canonico: *Significance of reheat cracks to the integrity of pressure vessels for light-water reactors*, United States: N. p., 1977.
- [31] R.D. Thomas: *Weld. J.*, 1984, vol. 63(12), pp. 355s-368s.
- [32] L. Li, R. W. Messler: *Weld. J.*, 2000, Vol 79, pp. 137s-144s.
- [33] I. Phung-On, *An investigation of reheat cracking in the weld heat affected zone of type 347 SS*, Doctoral dissertation, The Ohio State University, 2007.
- [34] R. Kant, *Stress relief cracking susceptibility in high temperature alloys*, Doctoral dissertation, Lehigh University, 2018.
- [36] H. Van Wortel, *Relaxation cracking in the process industry, an underestimated problem*, *BALTICA 4 - Plant Maintenance for Managing Life and Performance*, 1998, vol. 2, pp. 637-647
- [37] J. G. Nawrocki, J. N. Dupont, C. V. Robino, J. D. Puskar, A. R. Marder: *Weld. J.*, 2003, vol. 82(2), pp. 25-34s
- [38] I. Dayalan, P. Crasta, S. Pradhan, R. Gupta: *A Review on Stress Relaxation Cracking in Austenitic Stainless Steel*, *Proceedings of International Conference on Intelligent Manufacturing and Automation. Lecture Notes in Mechanical Engineering*. Springer, Singapore 2020.  
[https://doi.org/10.1007/978-981-15-4485-9\\_44](https://doi.org/10.1007/978-981-15-4485-9_44)
- [39] S. He, H. Shang, A. Fernández-Caballero, A.D. Warren, D.M. Knowles, P.E.J. Flewitt, T.L. Martin: *Mat. Sci. Eng. A*, 2021, vol. 807, pp. 140859
- [40] H. Stahl, G. Smith, S. Wastiaux: *J. Fail. Anal. and Preven.* 2000, vol. 1, pp. 51-54,
- [41] C. J. Middleton: *Metal. Sci.*, 1981, vol. 15:4, pp. 154-167
- [42] S. Bradley, *Stress Relaxation Cracking, a Forgotten Phenomenon*, *CorrosionPedia*, 2021, [www.corrosionpedia.com](http://www.corrosionpedia.com).
- [43] K. Mariappan, V. Shankar, A. K. Bhaduri: *Mater. High. Temp.*, 2020, vol. 37:2, pp. 114-128
- [44] X. Xiao, D. Li, Y. Li, S. Lu: *J. Mater. Sci. Technol.*, 2022, vol. 100, pp. 82-90
- [45] P.J. Bouchard, P.J. Withers, S.A. McDonald, R.K. Heenan: *Acta Mater.*, 2003, Vol.52, pp. 23-34
- [46] T. Burnett, R. Geurts, H. Jazaeri, S. Northover, S. McDonald, S. Haigh, R. Bouchard, P. Withers: *Mater. Sci. Technol.* 2015, vol. 31, 522-534
- [47] H. Jazaeri, P. Bouchard, M. Hutchings, A. Mamun, R. Heenan: *Conference: 13th International Conference on Creep and Fracture of Engineering Materials and Structures at: Toulouse, France*, 2015.
- [48] H. Jazaeri, P. Bouchard, M. Hutchings, A. Mamun, R. Heenan: *Procedia Struct. Integr.*, 2016, vol.2, pp. 942-949
- [49] H. Jazaeri, P. Bouchard, M. Hutchings, M. Spindler, A. Mamun, R. K. Heenan: *Metals*, 2019, vol. 9, pp.318
- [50] P. Palanichamy, M. Vasudevan, T. Jayakumar : *Sci. Technol. Weld. Join.*, 2009, vol. 14:2, pp. 166-171

- [51] H. X. Yuan, Y. Q. Wang, Y. J. Shi, L. Gardner: *Thin-Walled Struct.*, 2014, vol.79, pp.38-51
- [52] P. Vasantharaja, M. Vasudevan, P. Palanichamy, *J. Manuf. Process.*, 2015, vol.19, pp. 187-193
- [53] J. L. Chaboche: *Int. J. Plast.*, 2008, vol.24, pp. 1642 – 1693
- [54] CEA, Cast3M, 2021, 2021. <http://www-cast3m.cea.fr/>.
- [55] S. I. Wright, M. M. Nowell, D. P. Field: *Microsc Microanal.*, 2011, vol. 17(3), pp. 316-29
- [56] J. A. Brooks, J. C. Williams, A. W. Thompson: *Metall. Mater. Trans. A*, 1983, vol. 14, pp. 1271–81
- [57] Grong, O: *Metallurgical Modelling of Welding*, 2nd. Edition, Institute of Materials, London, UK, 1997
- [58] Y. Jiang, Y. Kan, H. Chen: *Metals*, 2022, vol. 12, pp. 116
- [59] K. Weman, 19 - the weldability of steel, *Welding Processes Handbook (Second Edition)*, Woodhead Publishing, 2012, pp. 191–206
- [60] V. Vijayanand, M. Vasudevan, V. Ganesan, P. Parameswaran, K. Laha, A. K. Bhaduri: *Metall. Mater. Trans. A*, 2016, vol. 47, pp. 2804-14
- [61] M. I. Isik, A. Kostka, V. A. Yardley, K. G. Pradeep, M. J. Duarte, P. P. Choi, D. Raabe, G. Eggeler: *Acta Mat.*, 2015, vol.90, pp. 94-104
- [62] I. Carneiro, S. Simões: *Metals*, 2020, vol. 10, pp. 1097
- [63] Y. E. F. Nippes, J. P. Balaguer: *Weld. J. Res Suppl.*, 1986, vol.65, pp. 237-243